

Copyright  
by  
Fernando Elias Osorio Perez  
2020

The Thesis Committee for Fernando Elias Osorio Perez  
certifies that this is the approved version of the following thesis:

**Harmonics Diversity Simulation of Inverter Based  
Generators in Large-Scale Power Systems**

APPROVED BY

SUPERVISING COMMITTEE:

---

Surya Santoso, Supervisor

---

Alex Q. Huang

**Harmonics Diversity Simulation of Inverter Based  
Generators in Large-Scale Power Systems**

by

**Fernando Elias Osorio Perez**

**THESIS**

Presented to the Faculty of the Graduate School of

The University of Texas at Austin

in Partial Fulfillment

of the Requirements

for the Degree of

**MASTER OF SCIENCE IN ENGINEERING**

THE UNIVERSITY OF TEXAS AT AUSTIN

May 2020

Dedicated to my parents, sister, and my uncle José

## Acknowledgments

I want to express my gratitude to my advisor, Dr. Santoso, for his continuous support towards the completion of my thesis, and his generous input in my training as a power systems engineer. I thank Dr. Huang for his power electronics lectures, and for reading this thesis.

I gratefully acknowledge my classmate Soham Roy, for his collaboration during this project. I also want to thank Robert F. Arritt from Electric Power Research Institute for his suggestions and feedback on the improvement of this work.

I thank the Fulbright-SENACYT-IFARHU scholarship for allowing me to study at The University of Texas at Austin. Without their support, I would not be able to meet all these great scholars.

# Harmonics Diversity Simulation of Inverter Based Generators in Large-Scale Power Systems

Fernando Elias Osorio Perez, M.S.E  
The University of Texas at Austin, 2020

Supervisor: Surya Santoso

This thesis explores the application of inverter-based generator (IBG) models in EMTP-RV. The main goal is to analyze how accurately different models can simulate the harmonic current spectra of an IBG, and study the interaction of the harmonic currents with the grid. The models to be studied are the detailed switch model (DM), harmonic averaged model (HAVM), and automated current source model (ACSM). In this work, the harmonic current diversity is also studied; the diversity arises from the different generating set-points of an IBG and the grid configuration at the point of interconnection (POI). Furthermore, the application of the ACSM in power systems with conventional generators is elaborated through a step-by-step procedure.

# Table of Contents

<b>Acknowledgments</b>	<b>v</b>
<b>Abstract</b>	<b>vi</b>
<b>List of Tables</b>	<b>ix</b>
<b>List of Figures</b>	<b>xi</b>
<b>Chapter 1. Introduction</b>	<b>1</b>
1.1 Motivation for a Simplified VSC Harmonic Model . . . . .	2
1.2 Thesis Outline . . . . .	2
<b>Chapter 2. Modeling IBGs as Detailed Switch Models</b>	<b>4</b>
2.1 Two-level Inverter Circuit Description . . . . .	5
2.2 Detailed Switch Model . . . . .	7
2.3 Harmonic Current Distortion Limits and Filters . . . . .	8
2.3.1 LC and LCL Filters . . . . .	9
2.4 dq Transform in EMTP-RV . . . . .	11
2.5 Phase Locked Loop . . . . .	14
2.5.1 PLL Model in EMTP-RV . . . . .	15
2.6 Control System . . . . .	18
2.6.1 Average Value Model . . . . .	19
2.6.2 VSC-Grid Plant Model . . . . .	20
2.6.3 Voltage-Mode Control . . . . .	22
2.6.4 Current-Mode Control . . . . .	24

<b>Chapter 3. Modeling IBGs as Automated Current Source Models</b>	<b>27</b>
3.1 Current Source Model . . . . .	27
3.2 Automated Current Source Model in EMTP-RV . . . . .	28
3.2.1 ACSM Algorithm . . . . .	31
3.3 Validation of the Automated Current Source Model in EMTP-RV	35
<b>Chapter 4. Modeling IBGs as Harmonic Averaged Value Models</b>	<b>41</b>
4.1 Harmonic Averaged Value Model . . . . .	41
4.2 Harmonic Averaged Model in EMTP-RV . . . . .	43
4.2.1 Harmonic Current Distortion Under Varying Power Factor	49
<b>Chapter 5. Harmonic Diversity Simulation</b>	<b>52</b>
5.1 69-kV Test Circuit Description . . . . .	52
5.2 Harmonic Diversity Simulation Using the Harmonic Average Value Model . . . . .	53
5.3 Harmonic Diversity Simulation Using the Automated Current Source Model . . . . .	62
<b>Chapter 6. Harmonics Diversity Simulation in Large-Scale Power Systems</b>	<b>71</b>
6.1 Modeling of Solar Farms in Transmission Systems . . . . .	71
6.2 Circuit Simulations with Multiple ACSMs . . . . .	74
6.2.1 Model with Solar Farms Rated at 30 MW . . . . .	77
6.2.2 Model with Solar Farms Rated at 100 MW . . . . .	80
<b>Chapter 7. Conclusion and Future Work</b>	<b>84</b>
7.1 Conclusion . . . . .	84
7.2 Future Work . . . . .	86
<b>Appendices</b>	<b>88</b>
<b>Bibliography</b>	<b>91</b>



## List of Tables

2.1	Maximum odd harmonic current distortion in percent of rated current $I_{rated}$ . . . . .	9
2.2	Maximum even harmonic current distortion in percent of rated current $I_{rated}$ . . . . .	9
2.3	Voltage-mode controller parameters . . . . .	24
2.4	Current-mode controller parameters . . . . .	25
3.1	DM LCL filter parameters at different generation levels. . . . .	36
4.1	Odd harmonic current magnitudes of HAVM and DM. P = 500 kW. . . . .	50
4.2	Odd harmonic current phase angles of HAVM and DM. P = 500 kW. . . . .	51
5.1	Current spectra of HAVM and DM at 500 kW (IBG1). . . . .	58
5.2	Current spectra of HAVM and DM at 250 kW (IBG2). . . . .	60
5.3	HAVM and DM fifth-order harmonic currents at BUS1. . . . .	60
5.4	Current spectra of ACSM and DM at 500 kW (IBG1, rated power). . . . .	65
5.5	Current spectra of ACSM and DM at 333 kW (IBG2, two-thirds of rated power). . . . .	65
5.6	ACSM and DM fifth-order harmonic currents at BUS1. . . . .	67
6.1	<i>base_ckt</i> generator plant parameters and power generation. . .	76
6.2	Results from <i>base_ckt</i> Load Flow and 30 MW-Rated ACSM Time Domain (TD, $h = 1$ ) Simulations - No Reactive Power Compensation. . . . .	78
6.3	Harmonic current magnitudes at BUS 2. Circuit with 30 MW rated solar farms (without reactive power compensation). . . .	78
6.4	Harmonic current phase angles at BUS 2. Circuit with 30 MW rated solar farms (without reactive power compensation). . . .	78

6.5	Results from <i>base_ckt_modified</i> Load Flow and 100 MW-Rated ACSM Time Domain (TD, $h = 1$ ) Simulations - with Reactive Power Compensation. . . . .	81
6.6	Harmonic current magnitudes at BUS 2. Circuit with 100 MW rated solar farms (with reactive power compensation). . . . .	81
6.7	Harmonic current phase angles at BUS 2. Circuit with 100 MW rated solar farms (with reactive power compensation). . . . .	82

## List of Figures

2.1	Single stage two-level inverter. . . . .	6
2.2	Base circuit one line diagram. . . . .	6
2.3	Simplified IGBT model. . . . .	7
2.4	Detailed switched model in EMTP-RV . . . . .	8
2.5	Left: LC filter, right: LCL filter. . . . .	10
2.6	$abc$ to $\alpha\beta\gamma$ transformation blocks in EMTP-RV. . . . .	13
2.7	Procedure to create a subcircuit in EMTP-RV. . . . .	13
2.8	PLL: (a) control diagram, (b) schematic diagram. . . . .	14
2.9	PLL circuit in EMTP-RV . . . . .	17
2.10	Subcircuit mask procedure in EMTP-RV . . . . .	18
2.11	Lossless AVM block diagram in $dq0 - frame$ . . . . .	20
2.12	Equivalent circuit in pu. . . . .	21
2.13	VSC model with LCL filter in stationary frame. . . . .	23
2.14	Voltage-mode controller schematic. . . . .	24
2.15	Current-mode control schematic. . . . .	26
3.1	CSM at the low voltage side of the transformer. . . . .	28
3.2	ACSM's internal current sources. . . . .	29
3.3	Flow diagram to create the ACSM from the DM. . . . .	31
3.4	Black box interface of the automated CSM. . . . .	33
3.5	Detailed switched model working with voltage-mode control. . . . .	36
3.6	Base circuit load flow model. . . . .	37
3.7	ACSM modeled at the POI. . . . .	38
3.8	ACSM and DM currents at high voltage side of transformer. P = 333 kW with pf = 1. . . . .	39
3.9	ACSM currents with $V_g \angle 0^\circ$ and $V_g \angle 30^\circ$ . P = 333 kW with pf = 1. . . . .	40
4.1	HAVM's voltage sources. . . . .	42

4.2	HAVM internal voltage sources. . . . .	44
4.3	SPWM and switching functions. . . . .	45
4.4	HAVM DC current model. . . . .	46
4.5	HAVM circuit. . . . .	47
4.6	HAVM and DM line to neutral terminal voltage. . . . .	48
4.7	HAVM and DM output current $I_L$ . . . . .	49
5.1	69-kV test circuit with two IBGs and a long transmission line. . . . .	54
5.2	Current measurements at BUS1 . . . . .	55
5.3	69 kV circuit with IBGs modeled using HAVMs. . . . .	56
5.4	Output current waveshapes comparison: HAVM (blue) and DM (blue). IBG1 (top), and IBG2 (bottom). . . . .	59
5.5	69 kV load flow circuit. . . . .	63
5.6	ACSM black box script in EMTP-RV, $P_{rated} = 500$ kW . . . . .	64
5.7	69-kV circuit with IBGs modeled using ACSMs. . . . .	68
5.8	69-kV circuit with IBGs modeled using DMs in voltage-mode control. . . . .	69
5.9	Output current waveshapes comparison: ACSM (blue) and DM (blue). IBG1 (top), and IBG2 (bottom). . . . .	70
6.1	Current output of: (i) 500 kW solar inverter (top), and (ii) 20 MW solar farm (bottom). . . . .	73
6.2	230-kV circuit with solar farm modeled as ACSMs: elements highlighted in yellow in <i>base_ckt</i> are replaced with elements highlighted in purple to obtain the TDLF model. . . . .	75
6.3	Current measurement sources at BUS 2. Circuit with 30 MW rated solar farms (without reactive power compensation). . . . .	79
6.4	Branches at BUS 2. Circuit with 100 MW rated solar farms (with reactive power compensation). . . . .	83
1	Current-mode control in EMTP-RV . . . . .	89
2	Voltage-mode control in EMTP-RV . . . . .	90

# Chapter 1

## Introduction

With the increasing integration of renewable sources into the power grid, the analysis of power systems during the planning phase is becoming more difficult. Non-linear loads and inverted-based generator plants (IBGs) inject harmonic currents into the grid – causing power quality issues. Furthermore, the modeling of IBG’s harmonic spectra is challenging, and detailed models usually require long run-times.

Some of the challenges in the computer simulation of IBGs are the presence of extreme nonlinearity in the semiconductors of voltage source converters (VSC), long simulation run-times, models that might not be accurate, and controllers dynamics [1]. Moreover, the scarcity of data related to filters and controllers provided by manufacturers makes it difficult to model new IBGs during the planning phase.

Different VSC model approaches have been studied in the literature [2–4]. Many of them successfully simulate the harmonic spectra of a VSC. However, the complexity of the models requires the tuning of multiple circuit and control components. The development of friendly VSC models will help in the analysis of harmonic currents and can enhance the implementation of

future harmonic mitigation strategies.

## **1.1 Motivation for a Simplified VSC Harmonic Model**

The need for IBG models during the planning phase that can read manufacturers' data, while having short run-times is the main motivation of this thesis. The accuracy and adaptability of VSC models are of great interest as well, since the VSC is a fundamental component of an IBG. Thus, the following VSC models will be studied in this thesis:

- Detailed switch model (DM).
- Harmonic average value model (HAVM)
- Automated current source model (ACSM)

The thesis also presents the application of a proposed automated current source model studied in [5]. Therefore, a procedure to run multiple IBGs in power systems with conventional generators is elaborated. This procedure aims to reduce the complexity of the simulation of IBGs during the planning phase.

## **1.2 Thesis Outline**

This thesis is organized into six chapters, as follows:

Chapter 1 introduces problems related to the harmonic modeling of IBGs and modeling alternatives for VSCs.

Chapter 2 discusses the theoretical background of VSC control and modeling. The detailed switch model is implemented in EMTP-RV.

Chapter 3 describes the automated current source model and its simulation using EMTP-RV.

Chapter 4 introduces the harmonic average model and its simulation using EMTP-RV.

Chapter 5 compares the performance of the studied models in a circuit with two IBGs.

Chapter 6 extends the analysis of the automated current source model and presents a procedure to run simulations with multiple IBGs in power systems with conventional generators.

Chapter 7 concludes the work presented in this thesis, gives final thoughts, and presents future work.

The Appendix provides other circuit diagrams developed for the thesis.

## Chapter 2

### Modeling IBGs as Detailed Switch Models

Electronic power conversion is extensively used in the power grid. Power electronic devices are not only a key element in the development of Distributed Generation Resources (DER), but also a prevalent component of conditioning, compensation, and active filtering [6]. Voltage Source Converters (VSCs) use power electronic switches to interface the DC and AC sides of the power system.

Two different VSC topologies are widely applied in DER; those are the two-level inverter and the three-level neutral-point clamped converter (NPC). The two-level inverter is the base circuit of this thesis since it is a simple but comprehensive model to analyze harmonic currents.

VSCs are interconnected with the grid through filters. These filters help reduce the total harmonic current distortion, keeping the IBGs within required harmonic limits. However, the filters have a significant impact on the VSCs' dynamics.

Consequently, the VSCs' controllers are designed using dynamic models that incorporate the filters and grid dynamics at the point of interconnection. A dynamic circuit of a two-level inverter is studied in this chapter, and the



parameters for the voltage-mode and current-mode control are computed using Simulink.

## 2.1 Two-level Inverter Circuit Description

DERs are usually connected to high voltage levels and supply significant power to the grid. Due to the power limitations of semiconductors, the inverter's legs contain multiple switches in series or parallel. Thus, the inverter can handle the required voltage and power generation. Inverters with multiple levels show a lower total harmonic distortion (THD) [7].

In the case of a two-level inverter, the converter comprises six switches in a three-leg configuration. Each leg of the inverter consists of two switches connected in series. The legs' operation is similar to that of the half-bridge single-phase inverter. The switches are turned on/off by a PWM signal; this signal uses a high-frequency carrier that is compared with a sinusoid. The output of the PWM block triggers the switches' gates.

The inverter's line-to-neutral output voltages have two different levels,  $\frac{+V_{dc}}{2}$  and  $\frac{-V_{dc}}{2}$  [6, 8]. Figure 2.1 shows a three-phase two-level inverter. The top switches are labeled S1, S2, and S3, while the bottom switches are S4, S5, and S6.

The complete IBG circuit shown in Figure 2.2 comprises a two-level single-stage converter, a filter (LC or LCL), and a 69 kV to 265 V three-phase transformer connected in delta-wye grounded configuration. The transformer

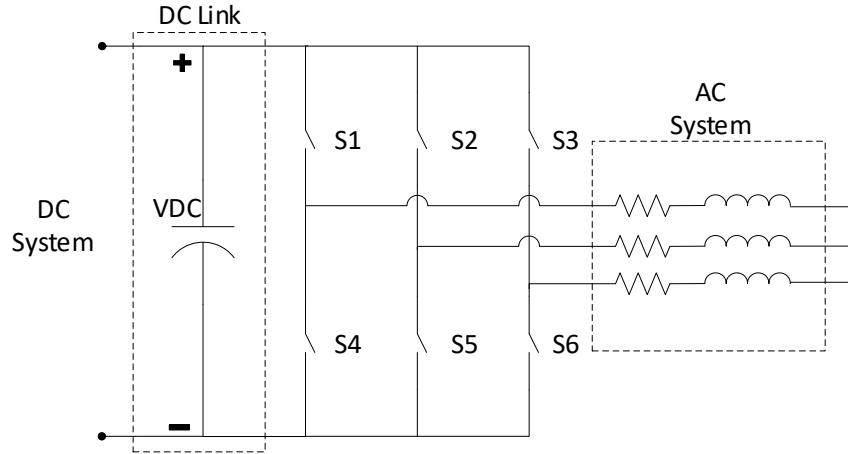


Figure 2.1: Single stage two-level inverter.

leakage reactance is  $X_{fmr} = 3\%$ . The system short-circuit strength at the POI is chosen to be 2000 MVA, equivalent to an inductance of 6.31 mH at 69 kV. The IBG DC source is modeled with a constant 600 V.

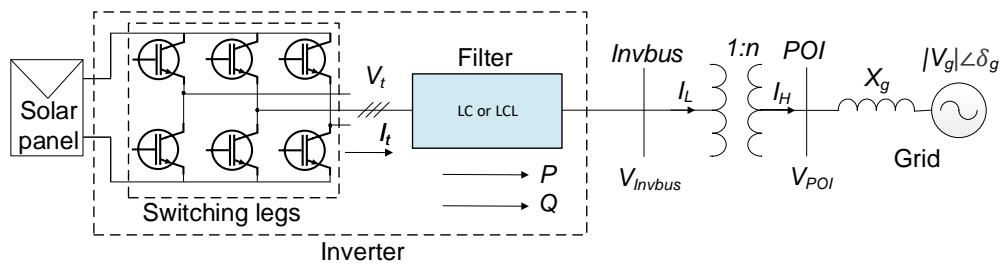


Figure 2.2: Base circuit one line diagram.

## 2.2 Detailed Switch Model

The detailed switch model (DM) uses IGBTs to model the switches in each leg. IGBTs are designed to operate like MOSFETs with a reduced on-state loss. The IGBT performance is between a MOSFET and a BJT, but it is faster compared to a BJT [1]. IGBTs are multipurpose commutation devices that can work in a wide range of voltages.

The DM accurately describes the dynamics and steady-state performance of a VSC. The DM's IGBTs can be modeled using a simplified approach, as shown in Figure 2.3. This simplified model of an IGBT shows a faster simulation run-time than the detailed version of the IGBT, while maintaining the high-frequency response of the DM.

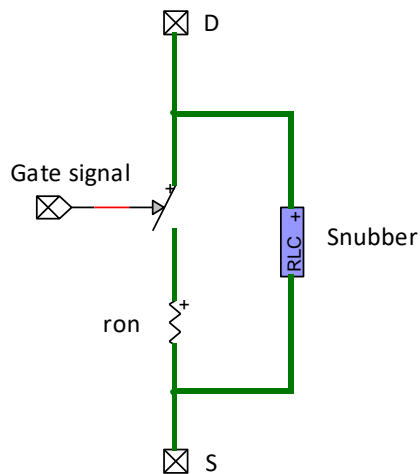


Figure 2.3: Simplified IGBT model.

Figure 2.4 shows the complete detailed switch model of a two-level inverter modeled in EMTP-RV. This circuit is used as a benchmark to compare the harmonic performance of the automated current source model and the harmonic average value model. The trigger signals of the IGBTs come from an SPWM block.

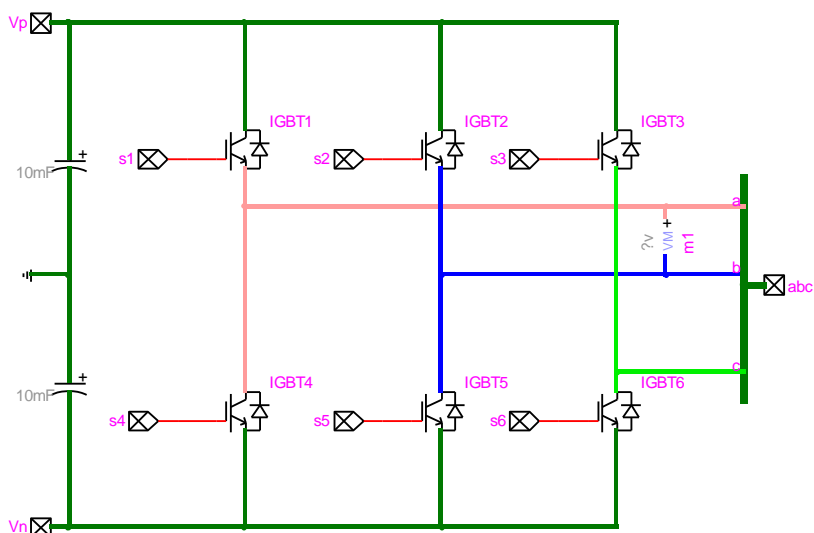


Figure 2.4: Detailed switched model in EMTP-RV

### 2.3 Harmonic Current Distortion Limits and Filters

Modulation techniques of power converters inject current harmonics into the grid; this current distortion causes several power quality issues at the distribution and transmission levels. Some of these issues are transient instability [9], changing fault current [10], and neutral conductor overload

[11].

The IEEE Standard 1547-2008 established the maximum distorted current limits. Table 2.1 and 2.2 show the odd and even current harmonic limits as a percentage of the rated current ( $I_{rated}$ ) [12].

Individual odd harmonic order $h$	$h < 11$	$11 \leq h < 17$	$17 \leq h < 23$	$23 \leq h < 35$	$35 \leq h < 50$
Percent (%)	4.0	2.0	1.5	0.6	0.3
Total rated current distortion (TRD) = 5.0 %					

Table 2.1: Maximum odd harmonic current distortion in percent of rated current  $I_{rated}$ .

Individual even harmonic order $h$	$h = 2$	$h = 4$	$h = 6$	$8 \leq h < 50$
Percent (%)	1.0	2.0	3.0	Specified in Table 26 [12]

Table 2.2: Maximum even harmonic current distortion in percent of rated current  $I_{rated}$ .

### 2.3.1 LC and LCL Filters

DER projects can implement passive filters at the output of their power converters. This helps to filter out unwanted harmonics and keep the current distortion within limits. Two of the most common filter configurations are LC (inductor-capacitor) and LCL (inductor-capacitor-inductor), shown in Figure 2.5. Both arrangements are low-pass filters and have to be tuned appropriately depending on the inverter's controller technology and the system's impedance

at the point of interconnection (POI).

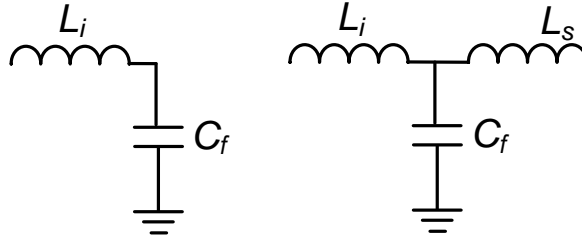


Figure 2.5: Left: LC filter, right: LCL filter.

An LC filter has an inductor  $L_i$  with typical values between 0.1 to 0.25 pu. To avoid unwanted resonance,  $C_f$  is designed to resonate at a higher frequency than the nominal frequency of the system but lower than the VSC switching frequency. The filter tank circuit is in parallel with the grid equivalent impedance at the POI. This impedance is also used in the computation of the filter's resonance frequency [2].

LCL filters achieve a higher attenuation level with lower price and size, but have the disadvantage that they can be highly unstable; this means that passive or active damping might be required. A comprehensive analysis of LCL filter tuning is presented in [13].

The cut-off frequency for both filters can be calculated using (2.1) and (2.2). In both cases, the filter resonance study requires addition of the grid equivalent impedance at the POI. Lumping the equivalent grid inductance into  $L_s$  can simplify the dynamic model and design process of VSC's controllers.

$$f_0 = \frac{1}{2\pi\sqrt{L_i C_f}} \quad (2.1)$$

$$f_0 = \frac{1}{2\pi} \sqrt{\frac{L_i + L_s}{L_i L_s C_f}} \quad (2.2)$$

## 2.4 dq Transform in EMTP-RV

The dq transformation is used to convert the current and voltage measurements from the *abc-frame* to the *dq0-frame*. The transformation is performed in two steps. First, the measured signals are converted from *abc-frame* to  *$\alpha\beta\gamma$ -frame* using (2.3) to (2.5). Then the  *$\alpha\beta\gamma$*  results are converted to *dq0* with (2.6) and (2.7). The angle  $\theta$  is obtained from a phase-locked loop (PLL).

$$V_\alpha = \frac{2}{3}(V_a - \frac{1}{2}V_b - \frac{1}{2}V_c) \quad (2.3)$$

$$V_\beta = \sqrt{\frac{1}{3}}(V_b - V_c) \quad (2.4)$$

$$V_\gamma = \frac{1}{3}(V_a + V_b + V_c) \quad (2.5)$$

$$V_d = \sin(\theta)V_\beta + \cos(\theta)V_\alpha \quad (2.6)$$

$$V_q = \cos(\theta)V_\beta - \sin(\theta)V_\alpha \quad (2.7)$$

The inverse transform is performed using (2.8) to (2.12). The zero component of the  $dq0$  –  $frame$  and the  $\gamma$  of  $\alpha\beta\gamma$  –  $frame$  are approximately zero in a balanced system.

$$V_\alpha = -\sin(\theta)V_q + \cos(\theta)V_d \quad (2.8)$$

$$V_\beta = \cos(\theta)V_q + \sin(\theta)V_d \quad (2.9)$$

$$V_a = V_\alpha + V_\gamma \quad (2.10)$$

$$V_b = -\frac{1}{2}(V_\alpha - \sqrt{3}V_\beta) + V_\gamma \quad (2.11)$$

$$V_c = -\frac{1}{2}(V_\alpha + \sqrt{3}V_\beta) + V_\gamma \quad (2.12)$$

The EMTP-RV function block  $f(u)$  can be used to implement these functions in EMTP-RV. Figure 2.6 shows how to use function blocks to create the  $abc$  to  $\alpha\beta\gamma$  transformation blocks. Multiple blocks can be added to a subcircuit.

Figure 2.7 shows the procedure to create subcircuit: first, select the elements to add to the subcircuit and then click on the “Options” tab followed by “Create Subcircuit Block...” which is under the “Subcircuit” section.



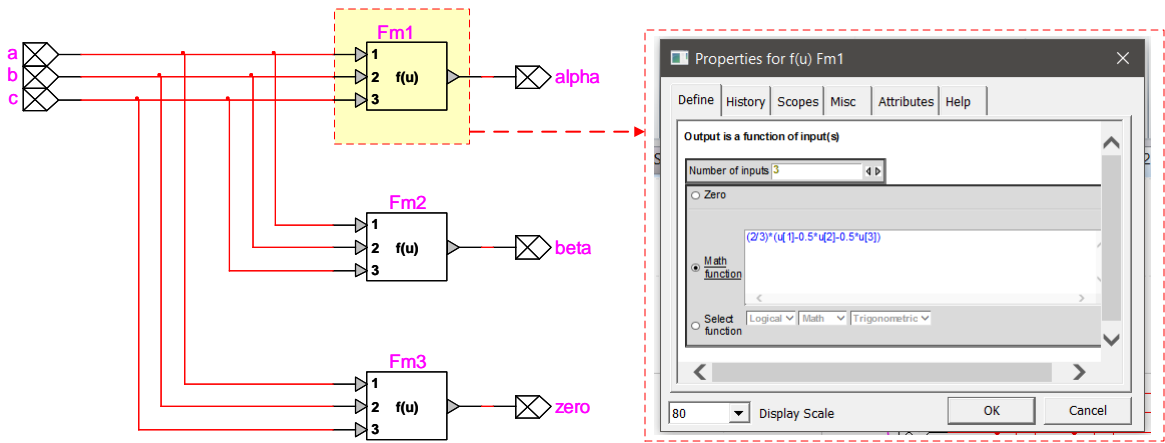


Figure 2.6:  $abc$  to  $\alpha\beta\gamma$  transformation blocks in EMTP-RV.

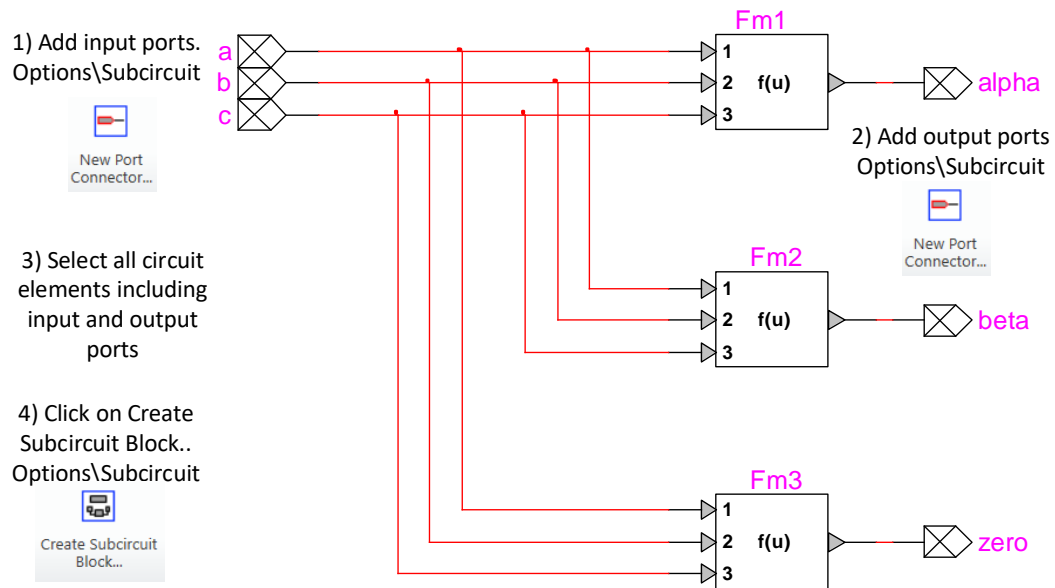


Figure 2.7: Procedure to create a subcircuit in EMTP-RV.

## 2.5 Phase Locked Loop

A PLL is required to synchronize the VSC in steady state and during transients. The POI phase voltage in  $dq0$ –*frame* can be modeled with (2.13) and (2.14). The PLL regulates  $\rho$  at  $\omega_o t + \theta_o$ . The parameter  $\rho$  is the phase-shift from  $V_g$  (slack source),  $\omega_o$  is the system angular velocity, and  $\theta_o$  is the source's initial phase angle. Figure 2.8 shows the control diagrams of a PLL [2, 6].

$$V_{s,d} = V_s \cos(\omega_o t + \theta_o - \rho) \quad (2.13)$$

$$V_{s,q} = V_s \sin(\omega_o t + \theta_o - \rho) \quad (2.14)$$

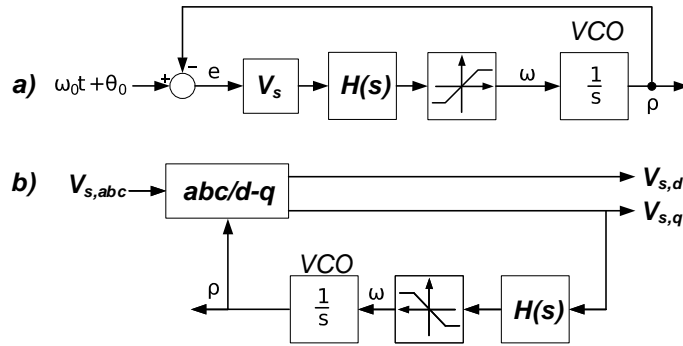


Figure 2.8: PLL: (a) control diagram, (b) schematic diagram.

The PLL loop gain is modeled using (2.15). The compensator ( $H(s)$ ) transfer function is shown in (2.16). It must include a pole at  $s = 0$  and a complex-conjugate at  $s = \pm j2\omega_o$ . The loop gain magnitude is designed to drop with a slope of  $-40$  dB/sec for  $\omega > 2\omega_o$ , with a double real pole at  $s = -2\omega_o$ .

The voltage  $V_{sn}$  is the nominal line-to-neutral voltage at the POI, and  $F(s)$  is a proper transfer function without a zero at the origin. The parameters  $h$  and  $F(s)$  are calculated depending on the stability requirements.

$$l(s) = \frac{V_s H(s)}{s} \quad (2.15)$$

$$H(s) = \frac{h}{V_{sn}} \frac{s^2 + (2\omega_o)^2}{s(s + 2\omega_o)^2} F(s) \quad (2.16)$$

### 2.5.1 PLL Model in EMTP-RV

To model the PLL in EMTP-RV it is required to compute the compensator transfer function from (2.16). The procedure is taken from [6] and modified to work at 265 V and 69 kV. The nominal frequency of the system is  $\omega_o = 2\pi 60$  rad/s.

Let us assume the required crossover frequency as  $\omega_c = 200$  rad/sec. To stabilize the system, a phase margin of  $60^\circ$  is used to calculate the closed loop phase angle. Replacing  $\omega_c$  in (2.15) and assuming  $hF(s) = 1$ , we get  $\angle l(j\omega_c) = -119.712^\circ$ . Thus, to achieve the desired  $60^\circ$  phase margin in the loop, it is required to add  $90^\circ$  to  $l(s)$ .

Two cascaded lead compensators can be used in  $F(s)$  to attain the phase margin as shown in (2.17) to (2.19). The angle  $\delta_m = 45^\circ$  is the phase of each lead compensator at  $\omega_c$ .

$$F(s) = \left( \frac{s + p/\alpha}{s + p} \right) \left( \frac{s + p/\alpha}{s + p} \right) \quad (2.17)$$

$$p = \omega_c \sqrt{\alpha} \quad (2.18)$$

$$\alpha = \frac{1 + \sin \delta_m}{1 - \sin \delta_m} \quad (2.19)$$

The resulting  $F(s)$  transfer function is shown in (2.20).

$$F(s) = \left( \frac{s + 83}{s + 482} \right)^2 \quad (2.20)$$

Now set  $|l(j\omega_c)| = 1$  and solve the closed loop equation. The resulting  $h$  is equal to 267478. The  $h$  result is independent of the nominal voltage and can be used for both the 265 V and 69 kV system. The resulting  $H(s)$  transfer function at 265 V and 69 kV are shown in (2.21) and (2.22) respectively.

$$H(s) = \frac{2.7 \times 10^{15} s^4 + 4.5 \times 10^{17} s^3 + 1.6 \times 10^{21} s^2 + 2.6 \times 10^{23} s + 1.1 \times 10^{25}}{2.2 \times 10^{12} s^5 + 5.4 \times 10^{15} s^4 + 5.0 \times 10^{18} s^3 + 2.0 \times 10^{21} s^2 + 3.0 \times 10^{23} s} \quad (2.21)$$

$$H(s) = \frac{5.3 \times 10^{15} s^4 + 8.9 \times 10^{17} s^3 + 3.1 \times 10^{21} s^2 + 5.0 \times 10^{23} s + 2.1 \times 10^{25}}{1.1 \times 10^{15} s^5 + 2.8 \times 10^{18} s^4 + 2.5 \times 10^{21} s^3 + 1.0 \times 10^{24} s^2 + 1.5 \times 10^{26} s} \quad (2.22)$$

Figure 2.9 shows the complete PLL circuit in EMTP-RV. The transfer function is modeled with an  $f(s)$  block, highlighted in yellow. The transfer function block's inputs are the polynomial coefficients in decreasing order of  $s$ . The transfer function coefficients and other parameters are inputs to the PLL's black box device with scripting, highlighted in red.

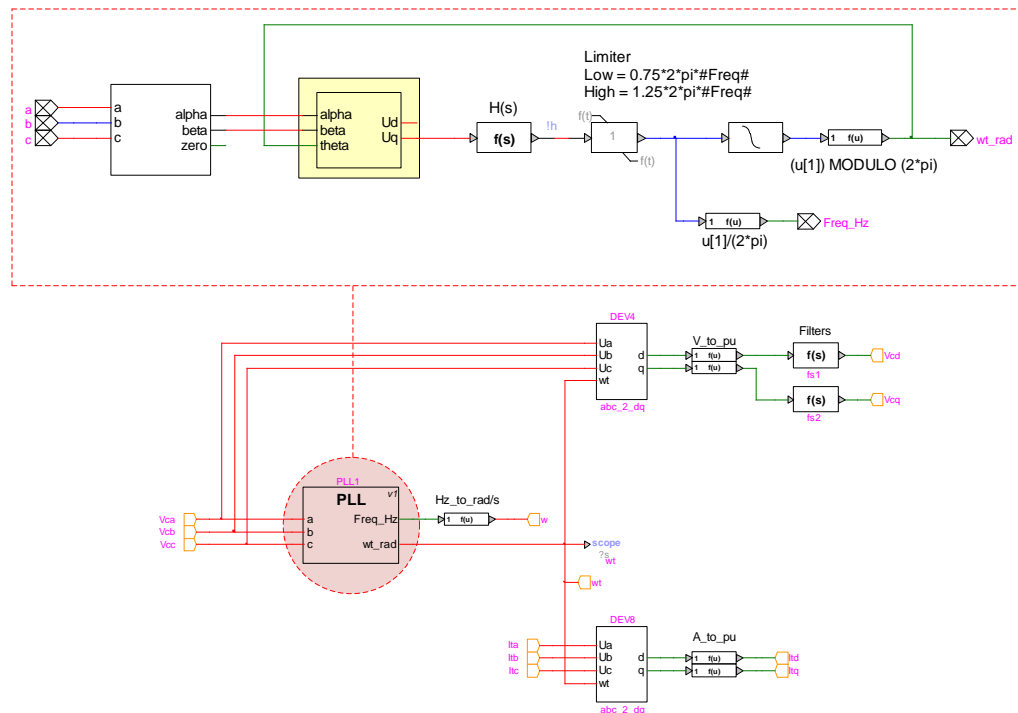


Figure 2.9: PLL circuit in EMTP-RV

Black box devices with scripting are easy to create using EMTP-RV. The procedure is similar to that of creating subcircuits from Section 2.4. After creating the subcircuit, right-click on the model subcircuit, then click on Properties, followed by “Subcircuit info...”. Next, click on the “Mask” tab

and check the “Mask this subnetwork” box, as shown in Figure 2.10. This will enable scripting for the black box, and let the user define initial parameters, rules, and variables to transmit to the subcircuit. EMTP-RV scripts use JavaScript commands.

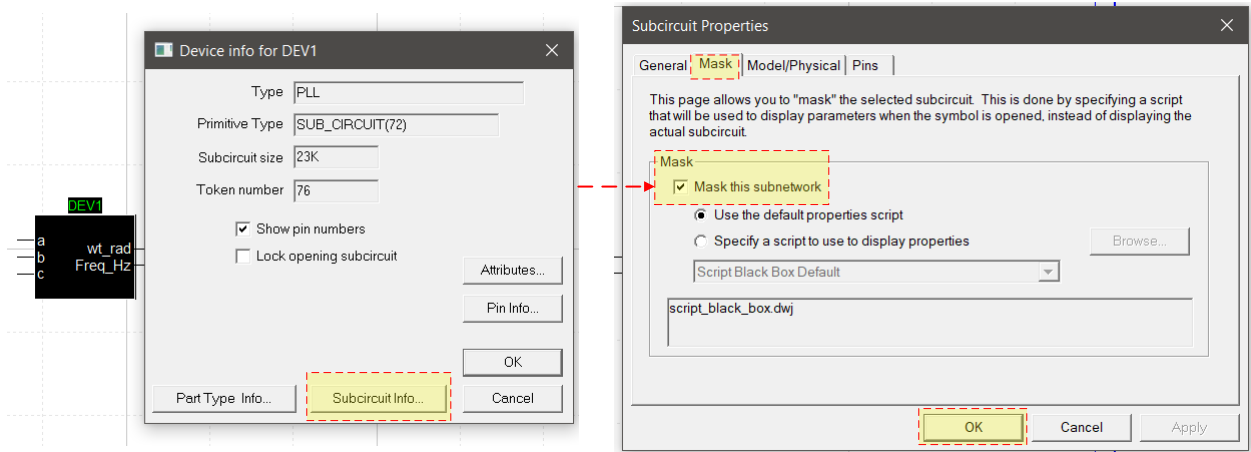


Figure 2.10: Subcircuit mask procedure in EMTP-RV

## 2.6 Control System

The VSC’s control system requires the tuning of multiple PI controllers. This is done by modeling the dynamic circuit in  $dq0 - frame$ . The dynamic circuit includes the dynamics of the filter and grid along with a simplified average model of the two-level inverter. Thus, the controller can be tuned using classic control theory or with the help of software like Simulink.

### 2.6.1 Average Value Model

The averaged value model (AVM) emulates the dynamics of a VSC operating at the nominal grid frequency [14]. The dynamic analysis of an AVM does not require knowledge about the high-frequency behavior of the detailed model. This is a valid simplification since the compensators and filters exhibit a low-pass characteristic. Thus, an AVM can successfully help in the design of controllers and dynamic analysis of a VSC operating at the nominal frequency of the grid. The AVM fundamental voltage of a two-level inverter is modeled using (2.23) to (2.25) [6].

$$V_{ta}(t) = \frac{m_a(t)V_{dc}}{2} - r_{on}i_{t,a}(t) \quad (2.23)$$

$$V_{tb}(t) = \frac{m_b(t)V_{dc}}{2} - r_{on}i_{t,b}(t) \quad (2.24)$$

$$V_{tc}(t) = \frac{m_c(t)V_{dc}}{2} - r_{on}i_{t,c}(t) \quad (2.25)$$

The component  $V_{t,a}(t)$ ,  $V_{t,b}(t)$ , and  $V_{t,c}(t)$  are the line-to-neutral voltages of the VSC. The signals  $m_a$ ,  $m_b$ , and  $m_c$  are the controller modulation signals. The VSC's on-losses are modeled using the parameter  $r_{on}$ . The currents  $i_{t,a}$ ,  $i_{t,b}$ , and  $i_{t,c}$  are the VSC's terminal currents.

Assuming on-resistances are small, a lossless AVM can be modeled in  $dq0$  – *frame*. To transform the terminal voltage equations from the  $abc$  – *frame* to the  $dq0$  – *frame* transformations from Section 2.4 are used. The resulting terminal voltages in the  $dq0$  – *frame* are shown in (2.26) and (2.27).

$$V_{t,d}(t) = \frac{m_d(t)V_{dc}}{2} \quad (2.26)$$

$$V_{t,q}(t) = \frac{m_q(t)V_{dc}}{2} \quad (2.27)$$

Figure 2.11 shows a lossless AVM block diagram modeled in the  $dq0$  – *frame*.

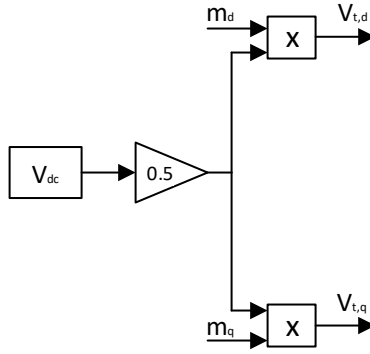


Figure 2.11: Lossless AVM block diagram in  $dq0$  – *frame*.

### 2.6.2 VSC-Grid Plant Model

The  $dq0$  – *frame* helps reduce the system complexity and the number of variables that will interact with the controller. Thus, the controller can avoid the tracking of sinusoidal references. This will allow the control system to incorporate PI compensators.



Figure 2.12a shows the equivalent network system in pu. As mentioned in Section 2.3.1, the equivalent system inductance is lumped with the filter impedance and modeled as a whole LCL system, as shown in Figure 2.12b.

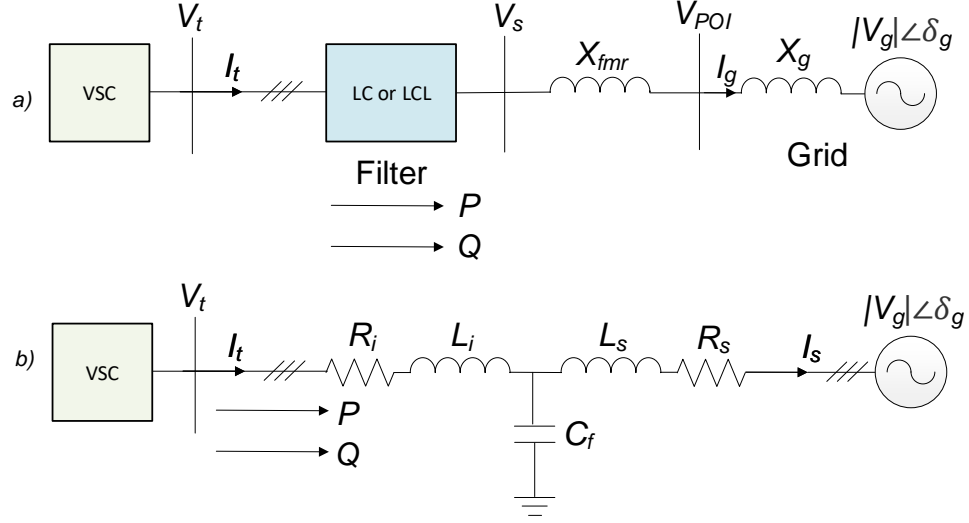


Figure 2.12: Equivalent circuit in pu.

The elements  $L_s$  and  $R_s$  denote the sum of the grid side impedances. This includes the filter, transformer, and the POI equivalent impedance. The elements  $L_i$  and  $R_i$  are the inverter side inductor and resistor.

The complete  $dq0$  circuit is developed using conventional circuit analysis as shown in (2.28) to (2.30).

$$L_i \frac{di_t}{dt} = V_t - R_i i_t - V_{C_f} \quad (2.28)$$

$$L_s \frac{di_s}{dt} = V_{C_f} - R_s i_s - V_g \quad (2.29)$$

$$C_f \frac{dV_{C_f}}{dt} = i_t - i_s \quad (2.30)$$

Equations (2.31) to (2.36) were obtained after manipulating (2.28) to (2.30) and applying the  $dq0$  transform.

$$L_i \frac{di_{t,d}}{dt} = \omega_o L_i i_{t,q} - R_i i_{t,d} - V_{C_f,d} + V_{t,d} \quad (2.31)$$

$$L_i \frac{di_{t,q}}{dt} = -\omega_o L_i i_{t,d} - R_i i_{t,q} - V_{C_f,q} + V_{t,q} \quad (2.32)$$

$$L_s \frac{di_{s,d}}{dt} = \omega_o L_s i_{s,q} - R_s i_{s,d} + V_{C_f,d} - V_{g,d} \quad (2.33)$$

$$L_s \frac{di_{s,q}}{dt} = \omega_o L_s i_{s,d} - R_s i_{s,q} + V_{C_f,q} - V_{g,q} \quad (2.34)$$

$$C_f \frac{dV_{C_f,d}}{dt} = \omega_o C_f V_{C_f,q} + i_{t,d} - i_{s,d} \quad (2.35)$$

$$C_f \frac{dV_{C_f,q}}{dt} = \omega_o C_f V_{C_f,d} + i_{t,q} - i_{s,q} \quad (2.36)$$

Figure 2.13 shows the Simulink dynamic circuit obtained by adding the average value model from Section 2.6.1 to the circuit equations in  $dq0$ . This model will be used to tune all the controllers using Simulink's control system tuner tool [15].

### 2.6.3 Voltage-Mode Control

Voltage-mode control is used in high voltage applications at the transmission level. The voltage-mode control adjusts the voltage magnitude and phase angle of the VSC's terminals using the POI voltage as a reference along with signals from the injected real and reactive power.

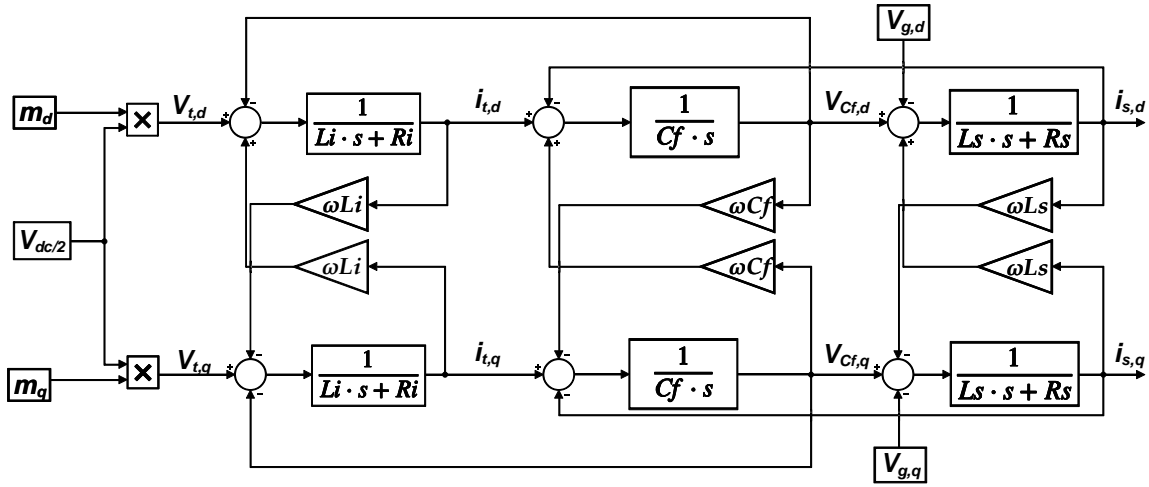


Figure 2.13: VSC model with LCL filter in stationary frame.

Voltage-mode control is easy to implement but has the drawback of not being able to limit the current at the VSC's terminals. This could cause fault current to flow through the VSC, causing damage to the equipment. In order to avoid damage to the VSC, a current limiting loop can be implemented, but it would increase the complexity of the controller. Other choices are available to achieve the current limiting feature in a simpler way [2, 6]. The voltage-mode control scheme is shown in Figure 2.14.

The voltage-mode controller is combined with the dynamic circuit of Figure 2.13. The filter is designed to emulate the harmonic spectra of an IBG operating at 500 kW with unity power factor. The filter parameters are  $L_i = 220 \mu\text{H}$ ,  $L_s = 240 \mu\text{H}$ , and  $C_f = 1900 \mu\text{F}$ . The resistors are neglected and the DC voltage is set to 600 V. Table 2.3 shows the computed controller parameters.

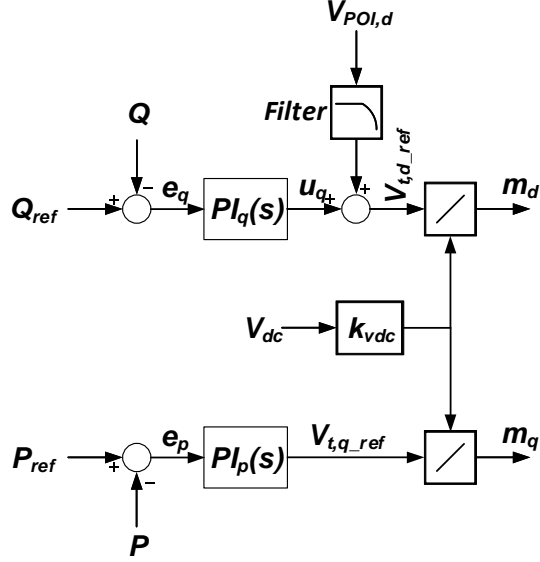


Figure 2.14: Voltage-mode controller schematic.

	$PI_q$	$PI_p$
$k_p$	10	10
$k_i$	5000	5000

Table 2.3: Voltage-mode controller parameters

#### 2.6.4 Current-Mode Control

The current-mode control achieves better performance during faults and transients compared to the voltage-mode control. The control loop adjusts the current injected into the grid by comparing it with a reference (set-point).

The output current is controlled by doing voltage modulation at the VSC's terminals. This is done by eliminating the coupled current components and the POI's voltage on (2.31) and (2.32). The controller Equations (2.37)

and (2.38) eliminate the aforementioned components and can be modeled as a control block diagram, as shown in Figure 2.15 [6, 16].

$$m_d = \frac{2}{V_{dc}}(PI_d(i_{t,dref} - i_{t,d}) - L\omega_o i_{tq} + V_{sd}) \quad (2.37)$$

$$m_q = \frac{2}{V_{dc}}(PI_q(i_{t,qref} - i_{q,d}) - L\omega_o i_{t,d} + V_{sq}) \quad (2.38)$$

The input signals of the controller can be transformed into pu. This will help to adjust the real power by controlling the peak of  $i_{t,d ref}$ . Moreover, the reactive power can be controlled with the negative peak of  $i_{t,q ref}$ . The real and reactive power control might require an external loop since this controller topology only controls the currents at VSC's terminals.

The current-mode controller is combined with the dynamic circuit of Figure 2.13. The filter parameters are  $L_i = 80 \mu\text{H}$  and  $C_f = 1500 \mu\text{F}$ . The resistors are neglected and the DC voltage is set to 600 V. Table 2.4 shows the computed controller parameters.

	$PI_d$	$PI_q$
$k_p$	10	10
$k_i$	200	200

Table 2.4: Current-mode controller parameters

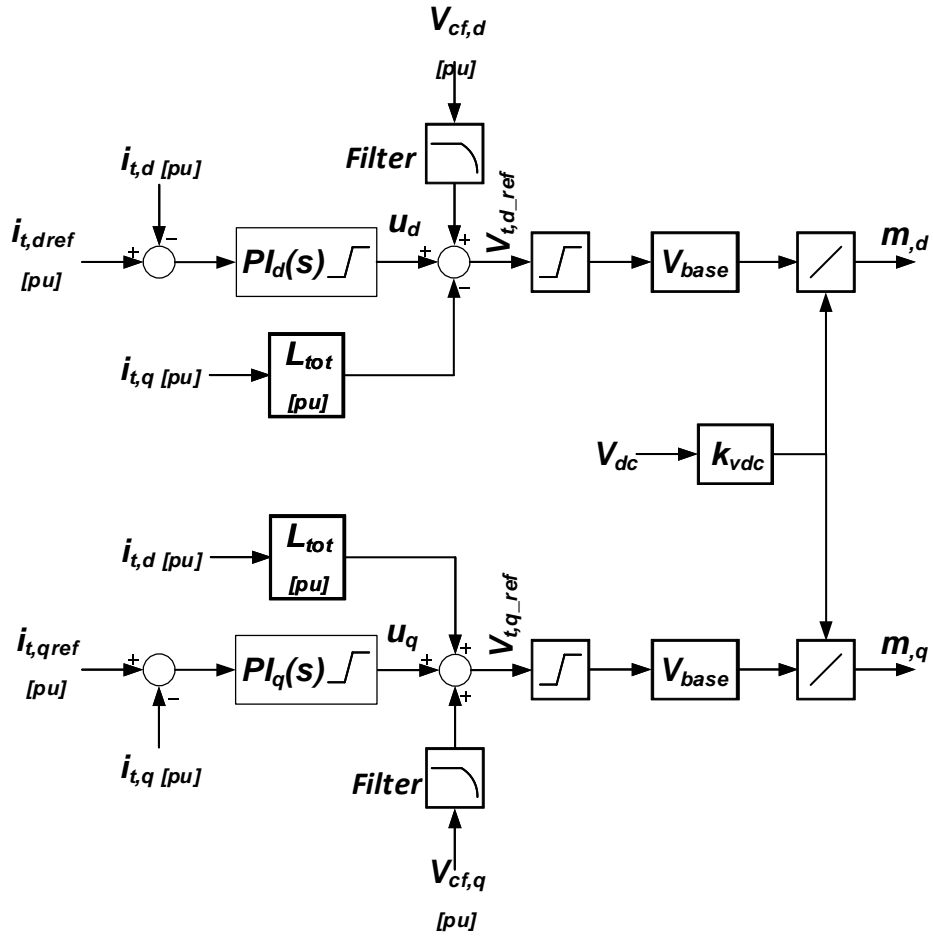


Figure 2.15: Current-mode control schematic.

## Chapter 3

# Modeling IBGs as Automated Current Source Models

IBGs can be modeled using multiple current sources. These current sources are assumed to be balanced and with constant harmonic current injection. The current source model has the advantage of not requiring a controller if the simulation is performed in a steady-state. This simplifies the implementation of the ACSM in large power systems.

### 3.1 Current Source Model

Current source models (CSMs) require data from manufacturers, and the voltage phase angle at the POI to adjust the current injected to the grid. The CSM comprises multiple current sources set to different harmonic frequencies. Harmonic current magnitudes are input as a percentage of the total  $I_{RMS}$ . Figure 3.1 shows a CSM modeled at the low voltage side of the transformer.

The CSM assumes a balanced current injection in all phases, meaning that the current injected into the grid is phase-shifted by  $120^\circ$  and  $-120^\circ$  for phases b and c, respectively. The harmonic impedances of the parallel current sources are hard to calculate and require data of the system at different

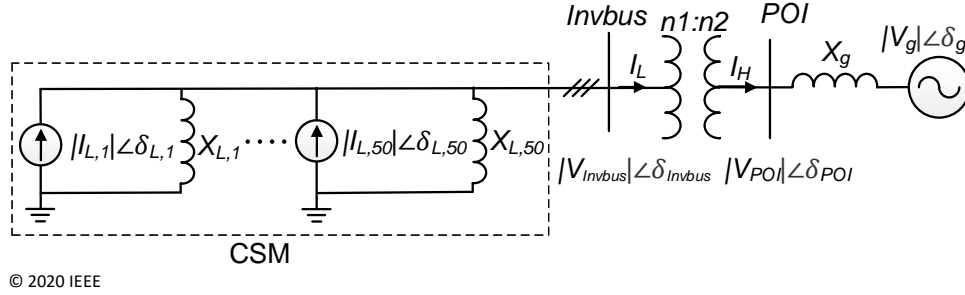


Figure 3.1: CSM at the low voltage side of the transformer.

states[17, 18]. Thus, to simplify the model, the impedance at each harmonic frequency is considered to be large and approximated as an open circuit.

### 3.2 Automated Current Source Model in EMTP-RV

The automated current source model studied in [5] is implemented using EMTP-RV. The circuit used in this section has the same electrical characteristics as the circuit described in Section 2.1.

The ACSM in EMTP-RV comprises multiple current sources connected in parallel, with each of them set to a different harmonic frequency ( $h = 1 \sim 50$ ) as shown in Figure 3.2. The ACSM's current sources read harmonic spectra data from a DWJ file. These data are obtained by measuring the harmonic currents at the filter's output or can also be obtained from a manufacturer's report. The measured currents are stored according to the IBG generation levels and transformer configurations. Harmonic current magnitudes are stored as a percentage of the total RMS current injected by the IBG.



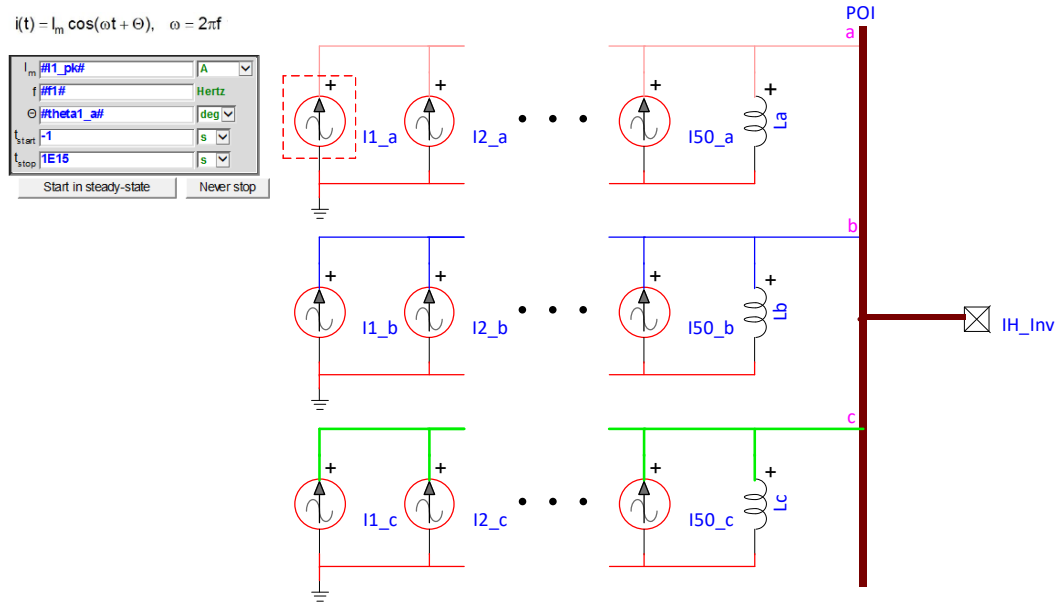


Figure 3.2: ACSM's internal current sources.

DWJ files use JavaScript and can be edited using text editors. The data are stored in arrays; each array corresponds to a particular generation level. The data for magnitudes and angles are stored in separated arrays, as shown in Algorithm 1.

---

**Algorithm 1** DWJ file structure

---

```
1: with(Math) {
2:   //DYg+30
3:   var mag_frac = new Array();
4:   //166kW
5:   mag_frac[0] = new Array(98.2059833732234, 0.084076001576418, ... );
6:   //333kW
7:   mag_frac[1] = new Array(99.2736612755428, 0.058603980589392, ... );
8:   //500kW
9:   mag_frac[2] = new Array(99.5347611449623, 0.044312109855935, ... );
10:  var ang = new Array();
11:  //166kW
12:  ang[0] = new Array(0.074696163, -89.99453778, 15.99397715, ... );
13:  //333kW
14:  ang[1] = new Array(-0.414910564, 37.29221973, -9.27862979, ... );
15:  //500kW
16:  ang[2] = new Array(-0.664570215, 127.4683835, 139.7796054, ... );
17: }
```

---

### 3.2.1 ACSM Algorithm

The ACSM is then modeled in EMTP-RV as a black box device with scripting. The black box is built in a similar way as the blocks described in Section 2.4 and 2.5.1. This script sets all current sources based on the fundamental voltage phase angle at Invbus (*inverter\_bus\_angle*), which is the bus right after the filter and before the transformer. A flow diagram to create the ACSM using data from a DM is shown in Figure 3.3

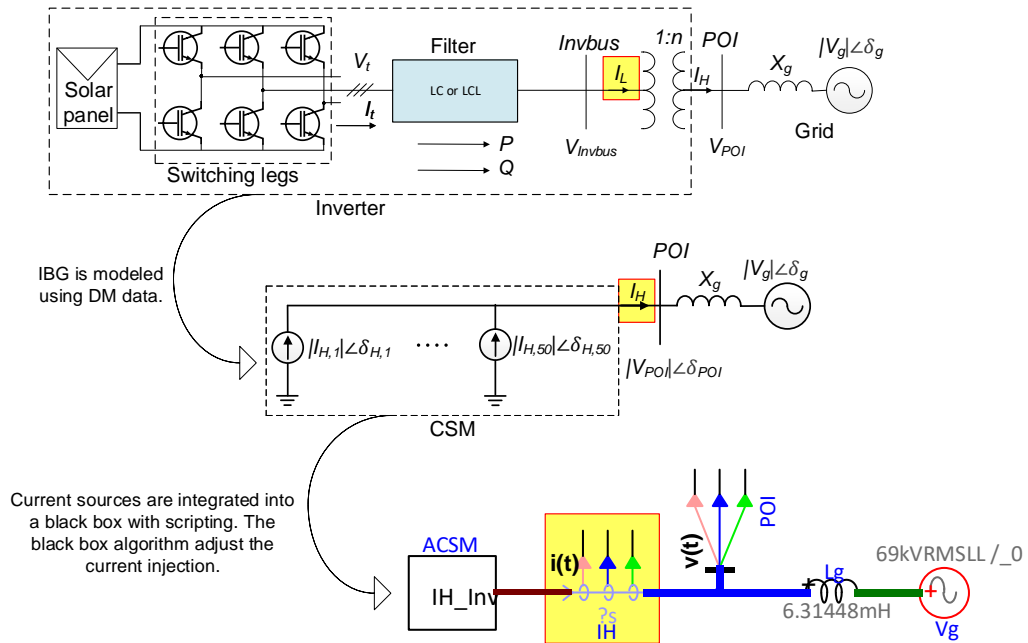


Figure 3.3: Flow diagram to create the ACSM from the DM.

Since the simulations in EMTP-RV always measure current phase an-

gles in the entire circuit with respect to a single reference node, a load flow (LF) program needs to be run in order to find the phase angle of the fundamental voltage at the inverter output node ( $\delta_{inv}$ ). This also needs to be fed to the CSM, so that it can adjust the phase angles such that they are referred to a common reference bus.

The CSM has two fixed parameters based on the inverter it represents: the rated generation level ( $P_{rated}$ ) and the line-to-line voltage of the inverter output bus ( $V_{inv,LL}$ ). At the time of simulation, the CSM black box can take certain inputs and produce the desired harmonic current profiles in a transmission system. The files `globalVariables_config.dwj` (*config: DYg/YYg*) store the current harmonic (1<sup>st</sup> to 50<sup>th</sup>) magnitude percentages and phase angles at the inverter output for every 1/3<sup>rd</sup> generation level from the DM. Manufacturer data may be used for magnitude percentages if available. Calculations are done within the CSM black box to obtain the phase angles (using load flow analysis) and magnitudes in a new system.

The EMTP black box model shown in Figure 3.4, can be provided with four inputs:

1. Input power fraction (*Pgen\_frac*: denoted as  $P_{frac}$  below)
2. Transformer turns ratio (*trans\_turns\_ratio*: denoted as  $n$  below)
3. Transformer configuration (*trans\_config*: denoted as *config* below)
4. Inverter bus phase angle to be obtained from LF (*inverter\_bus\_angle*: denoted as  $\delta_{inv}$  below)

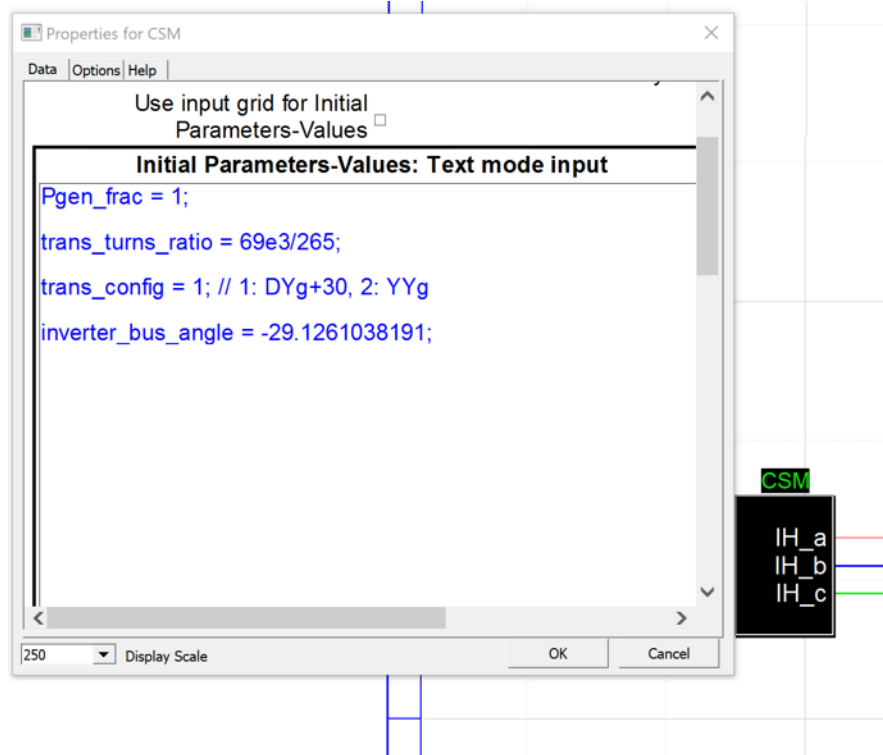


Figure 3.4: Black box interface of the automated CSM.

The black box code extracts inverter output bus harmonic current percentages ( $|I_{L,h}|%$ ) and phase angles ( $\delta_{L,h(inv)}$ ) of phase A from the DWJ files, and converts them to equivalent currents ( $|I_{H,h}| \angle \delta_{H,h(A,B,C)}$ ) at the POI. The algorithm for converting the available data to CSM equivalent current sources is listed in Algorithm 2.

---

**Algorithm 2** Algorithm for converting available data to CSM equivalent current sources.

---

```

1:  $P = P_{frac} \times P_{rated}$ 
2:  $I_{L,rms} = \frac{P}{\sqrt{3}V_{inv,LL}}$ 
3:  $I_{H,rms} = \frac{I_{L,rms}}{n}$ 
4: for  $h = 1, 2, \dots, 50$  do
5:   if  $h = 3, 6, 9 \dots$  (triplen) then
6:      $|I_{H,h}| = 0$ ;  $\delta_{H,h}$  does not matter
7:   else
8:      $|I_{H,h}| = I_{H,rms} \times |I_{L,h}|%$ 
9:      $\delta_{L,h} = \delta_{L,h(inv)} + h\delta_{inv}$ 
10:    if  $config=YYg$  then
11:       $\delta_{H,h} = \delta_{L,h}$ 
12:    else if  $config=DYg$  then
13:      if  $h = 2, 5, 8 \dots$  (negative sequence) then
14:         $\delta_{H,h} = \delta_{L,h} - 30^\circ$ ;  $\delta_{H,h(B,C)} = \delta_{H,h} \pm 120^\circ$ 
15:      else if  $h = 1, 4, 7 \dots$  (positive sequence) then
16:         $\delta_{H,h} = \delta_{L,h} + 30^\circ$ ;  $\delta_{H,h(B,C)} = \delta_{H,h} \mp 120^\circ$ 
17:      end if
18:    end if
19:  end if
20: end for

```

---

An example is shown below:

$$P_{rated} = 500 \text{ kW}$$

$$V_{inv,LL} = 265 \text{ V}$$

Inputs:  $P_{frac} = 1$   
 $n = \frac{69 \times 10^3}{265}$   
 $config = DYg$   
 $\delta_{inv} = -29.18^\circ$  (obtained from LF run)

For 5<sup>th</sup> harmonic ( $h = 5$  i.e. negative sequence):

From globalVariables\_DYg.dwj:  $|I_{L,h}| \% = 3.6653\%$ ,  $\delta_{L,h(inv)} = -13.04^\circ$

Calculations:  $P = P_{frac} \times P_{rated} = 500$  kW  
 $I_{L,rms} = \frac{P}{\sqrt{3}V_{inv,LL}} = 1089.34$  A  
 $I_{H,rms} = \frac{I_{L,rms}}{n} = 4.1837$  A  
 $\delta_{L,h} = \delta_{L,h(inv)} + h\delta_{inv} = -158.92^\circ$   
 $|I_{H,h}| = I_{H,rms} \times |I_{L,h}| \% = \mathbf{15.3344}$  A  
 $\delta_{H,h} = \delta_{H,h(A)} = \delta_{L,h} - 30^\circ = -188.92^\circ = 171.08^\circ$   
 $\delta_{H,h(B)} = \delta_{H,h(A)} + 120^\circ = -68.92^\circ$   
 $\delta_{H,h(C)} = \delta_{H,h(A)} - 120^\circ = 51.08^\circ$

### 3.3 Validation of the Automated Current Source Model in EMTP-RV

Let us compare the ACSM with a DM. The DM shown in Figure 3.5 is modeled as a 500 kW (rated power) two-level inverter with LCL filter parameters as shown in Table 3.1. The DM can operate at 500 kW (rated), 333 kW (two-thirds of rated power), and 166 kW (one-third of rated power) with pf=1.

Currents are measured at the output of the DM's filter. The currents

magnitudes and phase angles are stored in a DWJ file. Consequently, the ACSM will also operate at the same generating levels as the DM.

Before running a time-domain simulation, the fundamental voltage phase angle at Invbus is computed in a steady-state. This angle is computed using a load flow circuit, as shown in Figure 3.6. For this test, the ACSM is set to operate with  $P = 333 \text{ kW}$  and  $Q = 0 \text{ kvar}$ . The resulting angle is  $-21.4980^\circ$ .

The IBG is then modeled using an ACSM. The circuit of Figure 3.5 is modified by replacing the inverter and transformer with an ACSM modeled at the 69 kV side of the circuit, as shown in Figure 3.7.

	$L_i$ [ $\mu H$ ]	$L_s$ [ $\mu H$ ]	$C_f$ [ $\mu F$ ]
166 kW pf = 1	240	220	2370
333 kW pf = 1	240	220	2390
500 kW pf = 1	220	240	1900

Table 3.1: DM LCL filter parameters at different generation levels.

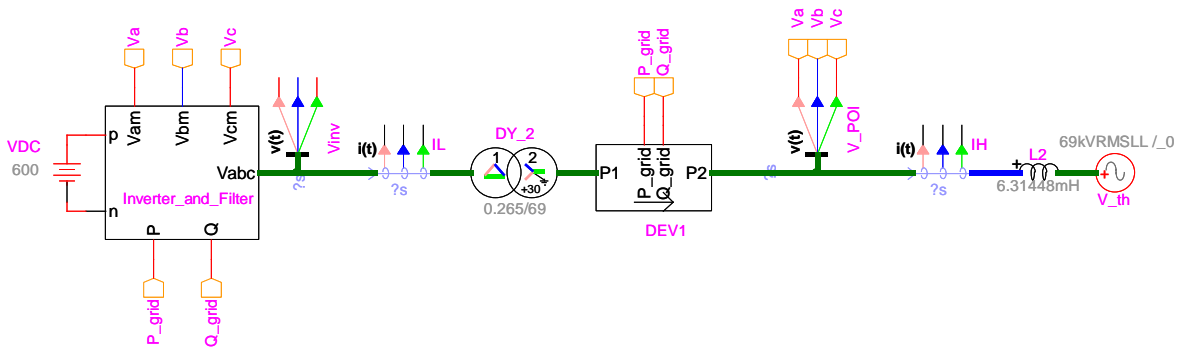


Figure 3.5: Detailed switched model working with voltage-mode control.



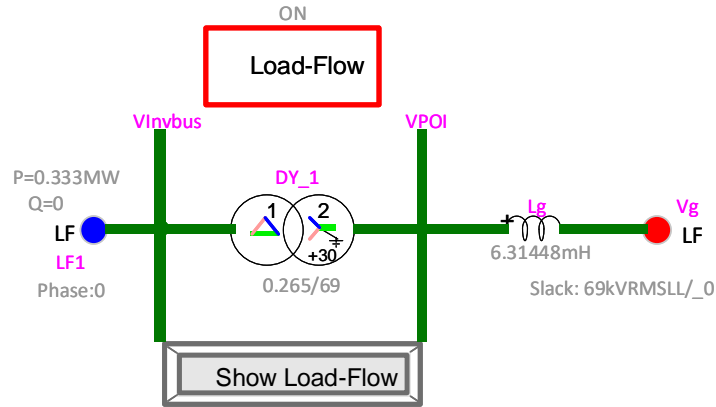


Figure 3.6: Base circuit load flow model.

The output currents of the ACSM and the DM operating at  $P = 333$  kW and  $\text{pf} = 1$  are shown in Figure 3.8. Both currents seem to be in phase, with similar harmonic distortions.

To validate the use of the *inverter\_bus\_angle* parameter to adjust the ACSM, the phase angle of the Thevenin source ( $V_g$ ) is adjusted to  $+30^\circ$ . Then, the load flow circuit is also adjusted to this new reference and a new *inverter\_bus\_angle* is computed. The resulting *inverter\_bus\_angle* is  $0.2900^\circ$ . The plots of the ACSM currents using  $V_g \angle 0^\circ$  and  $V_g \angle 30^\circ$  are shown in Figure 3.9

The ACSM uses fewer elements than the DM and can read the manufacturer's data (if available) to model IBGs at different locations. This makes the ACSM an attractive alternative to simulate IBGs during the planning stage. The ACSM could not perfectly emulate the DM since it assumes a bal-

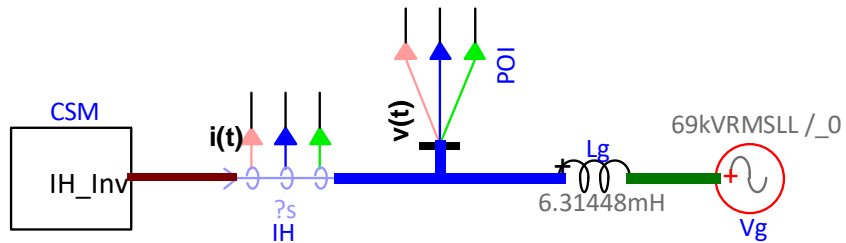


Figure 3.7: ACSM modeled at the POI.

anced condition in the injected currents, whereas in the DM some unbalanced currents can be observed. The DM unbalance results from the switching and power control in each leg of the inverter. Additionally, the transformer models of IBGs are simplified to avoid modeling the parallel impedance of harmonic current sources. These impedances require extensive computation and might change at different operating points.

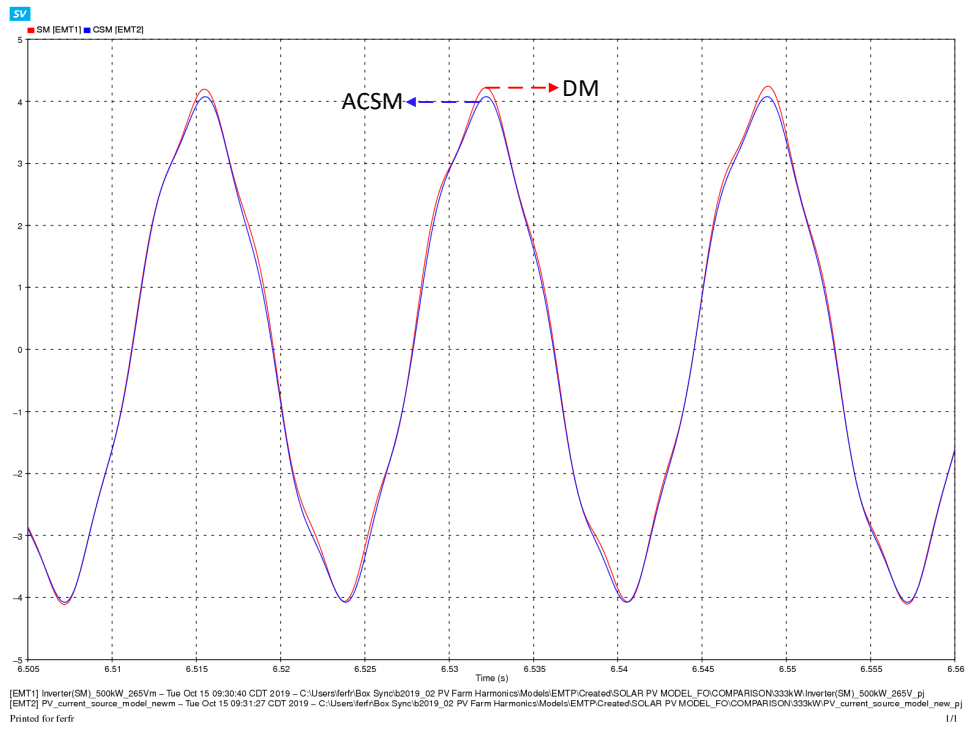


Figure 3.8: ACSM and DM currents at high voltage side of transformer.  
 $P = 333 \text{ kW}$  with  $\text{pf} = 1$ .

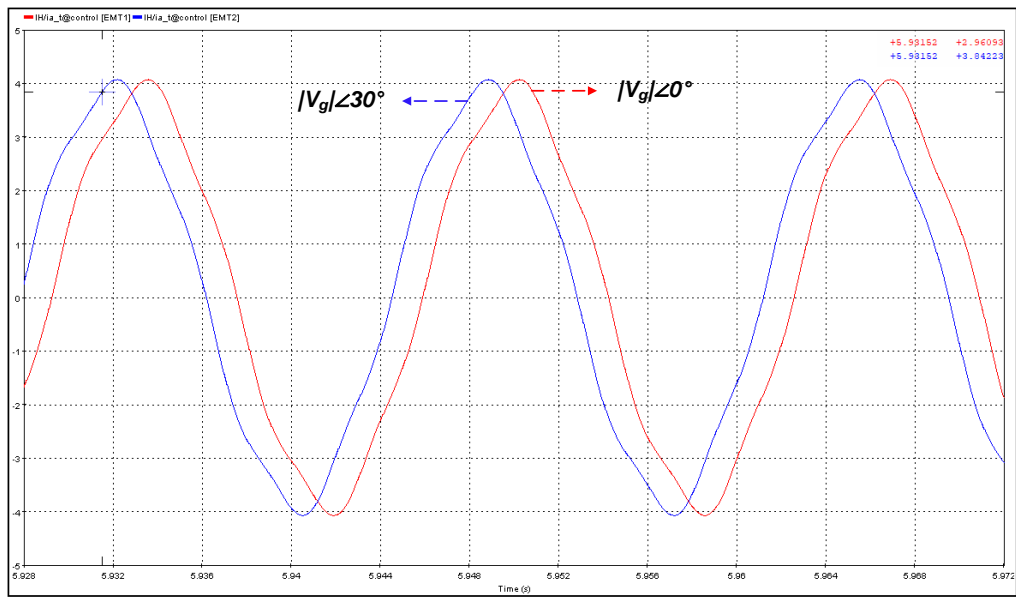


Figure 3.9: ACSM currents with  $V_g \angle 0^\circ$  and  $V_g \angle 30^\circ$ .  
 $P = 333 \text{ kW}$  with  $\text{pf} = 1$ .

## Chapter 4

# Modeling IBGs as Harmonic Averaged Value Models

In this chapter, the application of a harmonic average model (HAVM) is described. Different approaches to simulate AVMs with harmonic spectra have been studied [3, 4, 19]. These models use voltage sources and modulation techniques to emulate the harmonic content of a DM.

The HAVM works in current-mode control instead of voltage-mode control. This will allow the model to be more flexible when controlling real and reactive power. Moreover, the use of current-mode control intrinsically limits the output current of the VSC.

The HAVM is modeled using EMTP-RV and compared with a DM. The circuit characteristics are the same as those previously described in Section 2.1.

### 4.1 Harmonic Averaged Value Model

The AVM discussed in Section 2.6.1 is unable to emulate the harmonic spectra of the DM of Section 2.2. Thus, the HAVM aims to model the harmonic current spectra of the DM by using harmonic modulation techniques.

Similar to the AVM, the HAVM uses voltage sources to model the VSC,

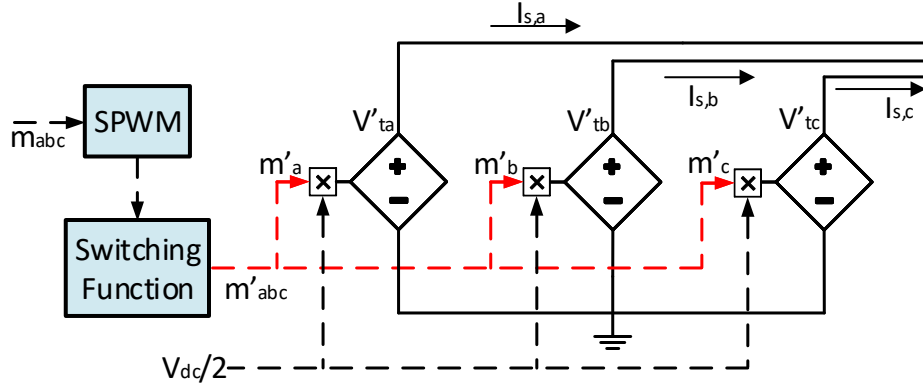


Figure 4.1: HAVM's voltage sources.

as shown in Figure 4.1. Voltages  $V'_{t,a}$ ,  $V'_{t,b}$ , and  $V'_{t,c}$  are the line-to-neutral terminal voltages of the VSC. These voltages are products of the switching function  $m'_n$  with  $\frac{V_{dc}}{2}$ . The HAVM terminals' voltages are modeled using (4.1) to (4.3).

$$V'_{ta}(t) = \frac{m'_a(t)V_{dc}}{2} \quad (4.1)$$

$$V'_{tb}(t) = \frac{m'_b(t)V_{dc}}{2} \quad (4.2)$$

$$V'_{tc}(t) = \frac{m'_c(t)V_{dc}}{2} \quad (4.3)$$

The switching functions are the mathematical difference of the upper and lower switch pulses (SU, SL). This function is modeled using (4.4) to (4.6).

$$m'_a = SU_a - SL_a \quad (4.4)$$

$$m'_b = SU_b - SL_b \quad (4.5)$$

$$m'_c = SU_c - SL_c \quad (4.6)$$

The upper and lower pulses are obtained from an SPWM block. The switching functions are limited to  $\pm 1$ . The phase  $a$  switches are (S1,S4), while phase  $b$  and phase  $c$  are (S2,S5) and (S3,S6) respectively. The two-level inverter DC current is modeled using (4.7).

$$I_{dc} = i_{ac,a}SU_a + i_{ac,b}SU_b + i_{ac,c}SU_c \quad (4.7)$$

## 4.2 Harmonic Averaged Model in EMTP-RV

The HAVM is modeled using EMTP-RV. Figure 4.2 shows the HAVM voltage sources. The on-state losses are modeled by placing a resistor at the output of each voltage source.

The SPWM block is modified by adding the switching functions blocks from (4.4) to (4.6). The switching functions subtract the SPWM output signals corresponding to upper and lower switches. The SPWM output is limited to  $\pm 1$  as shown in Figure 4.3.

The DC current of the HAVM is modeled using (4.7), as shown in Figure 4.4. The HAVM, filter, and controller are packed in a black box device with scripting as shown in Figure 4.5.

Next, let us compare the HAVM with a DM. Both the HAVM and DM work in current-mode control. The HAVM's terminal voltages are obtained by multiplying the switching functions with the DC voltage. Since the switching

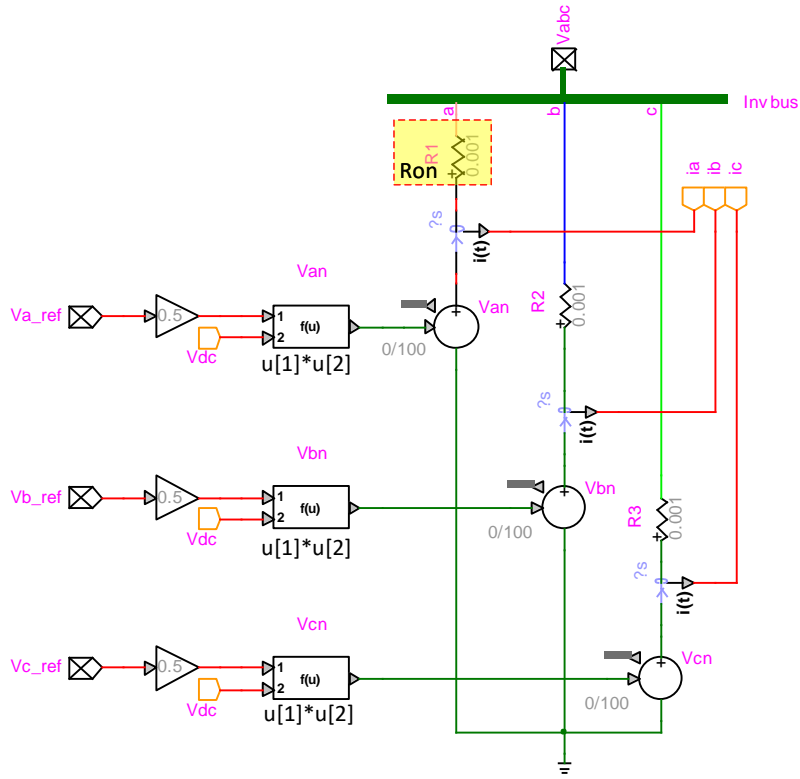


Figure 4.2: HAVM internal voltage sources.

function outputs are square wave signals, the HAVM's resulting terminal voltages are similar to that of the DM, as shown in Figure 4.6. It is observed that the HAVM voltage is lagging the DM. This delayed response of the HAVM affects the harmonic injection and might cause some differences in the total harmonic current distortion.

Current measurements were taken at the output of both the HAVM and the DM. Figure 4.7 shows the current measurements at the low voltage side



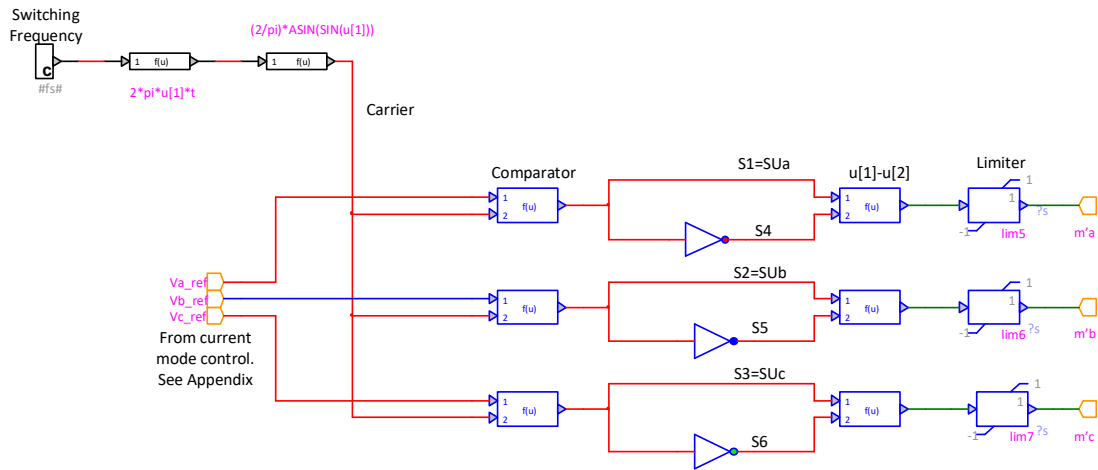


Figure 4.3: SPWM and switching functions.

of the transformers ( $I_L$ ). The HAVM current seems to be lagging the DM, similar to the previously discussed issue on the HAVM's terminal voltages. This could be the result of the slow response of the voltage sources w.r.t the controller signals.

The current plot shows a dominant fifth-order harmonic current in both models.

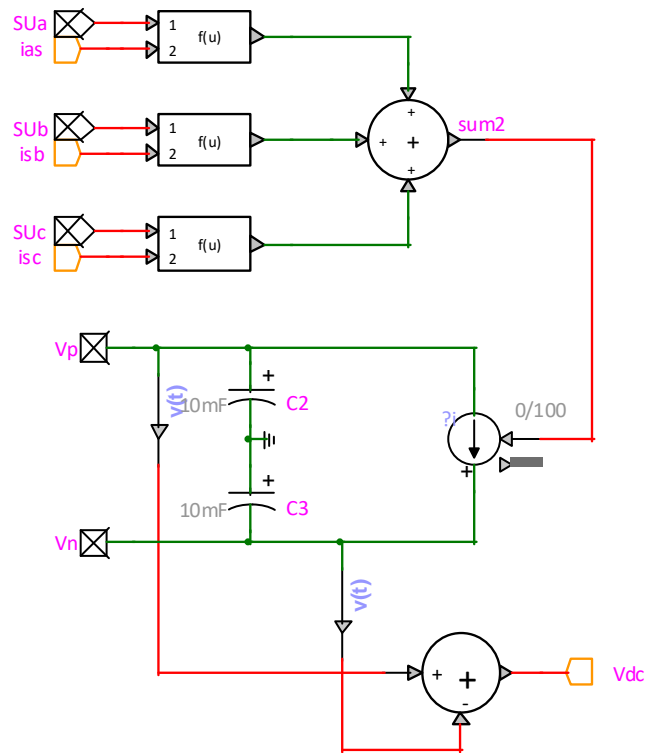


Figure 4.4: HAVM DC current model.

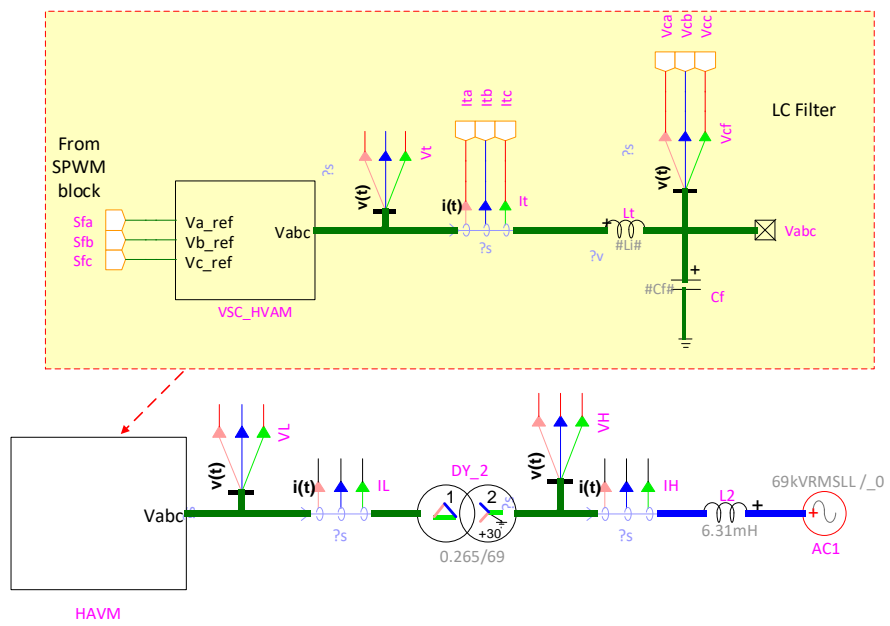


Figure 4.5: HAVM circuit.

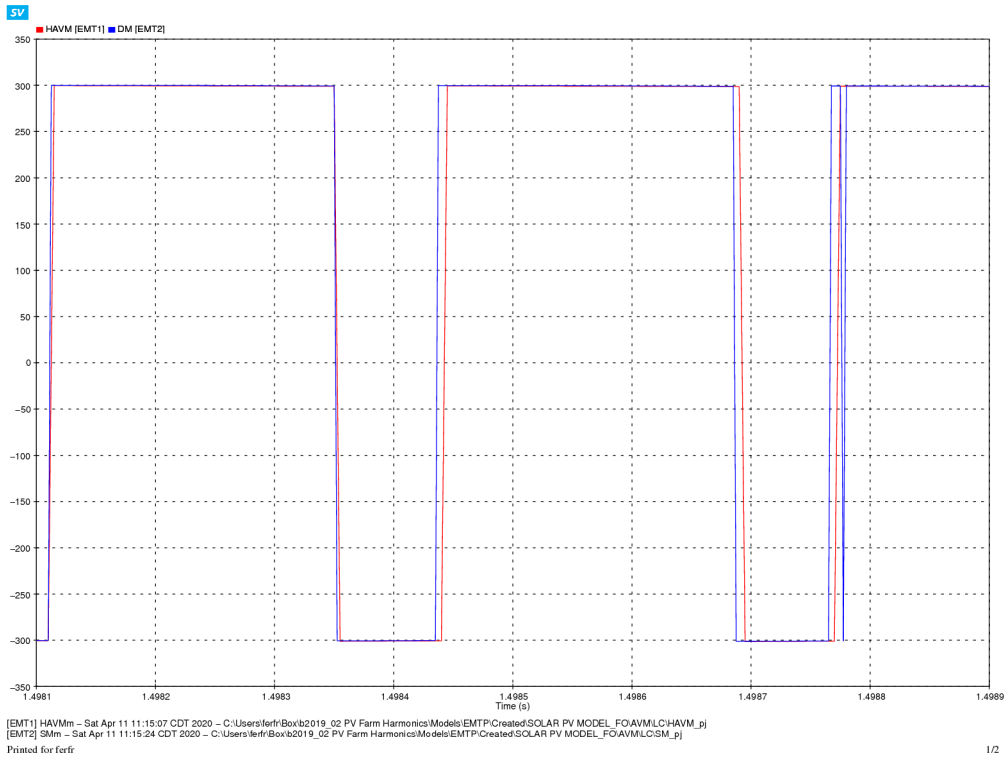


Figure 4.6: HAVM and DM line to neutral terminal voltage.

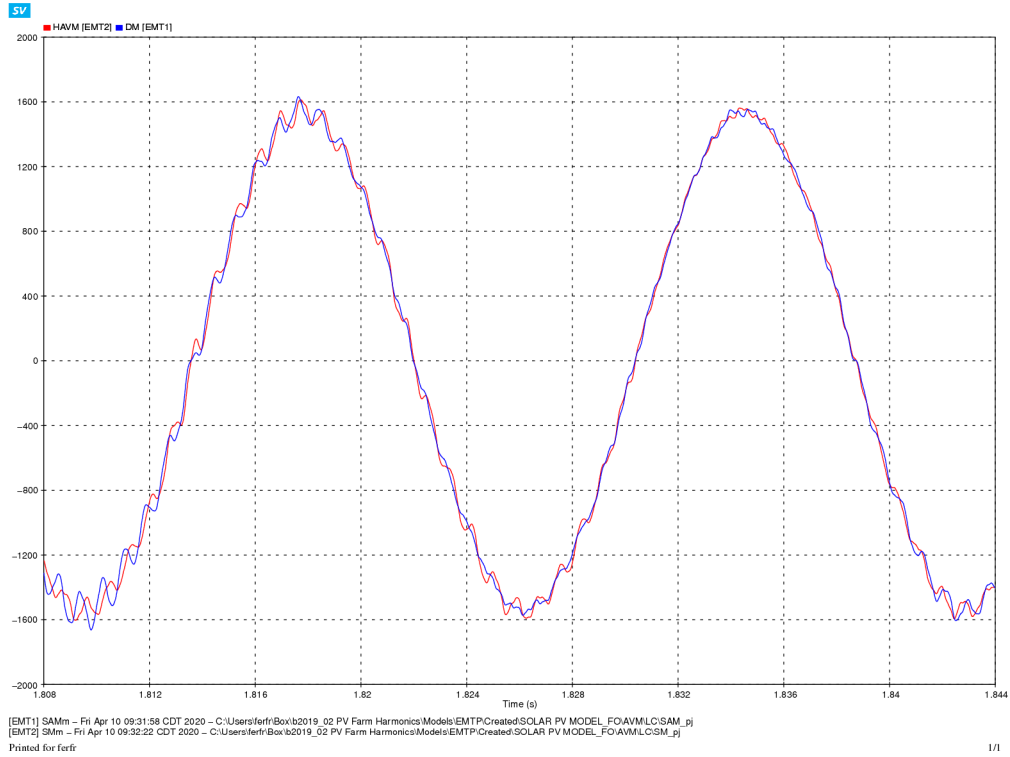


Figure 4.7: HAVM and DM output current  $I_L$ .

#### 4.2.1 Harmonic Current Distortion Under Varying Power Factor

The simulation of an IBG injecting reactive power into the grid is performed. The real power injection of the IBG is kept constant while the power factor is adjusted to different set-points. The HAVM and DM are compared to verify that both models interact similarly with the grid.

The HAVM and DM are set to generate a fixed real power of 500 kW.

Then, power factor is adjusted to  $\text{pf} = 1$ ,  $\text{pf} = 0.90$ ,  $\text{pf} = 0.80$ , and  $\text{pf} = 0.70$ . The harmonic current is measured at the low voltage side of the transformer ( $I_L$ ). Measured harmonics are  $h = 1 \sim 5$ , results are shown in Table 4.1 and 4.2.

	$I_{L,pk}$ with $\text{pf} = 1$ [A]		$I_{L,pk}$ with $\text{pf} = 0.9$ [A]	
h	HAVM	DM	HAVM	DM
1	$1.54 \times 10^{+03}$	$1.49 \times 10^{+03}$	$1.57 \times 10^{+03}$	$1.57 \times 10^{+03}$
3	$2.39 \times 10^{+00}$	$1.51 \times 10^{+00}$	$2.77 \times 10^{+00}$	$1.31 \times 10^{+00}$
5	$9.35 \times 10^{+00}$	$1.17 \times 10^{+01}$	$1.19 \times 10^{+01}$	$1.38 \times 10^{+01}$
	$I_{L,pk}$ with $\text{pf} = 0.8$ [A]		$I_{L,pk}$ with $\text{pf} = 0.7$ [A]	
h	HAVM	DM	HAVM	DM
1	$1.65 \times 10^{+03}$	$1.68 \times 10^{+03}$	$1.74 \times 10^{+03}$	$1.78 \times 10^{+03}$
3	$2.99 \times 10^{+00}$	$1.01 \times 10^{+00}$	$3.26 \times 10^{+00}$	$1.12 \times 10^{+00}$
5	$1.25 \times 10^{+01}$	$1.43 \times 10^{+01}$	$1.35 \times 10^{+01}$	$1.50 \times 10^{+01}$

Table 4.1: Odd harmonic current magnitudes of HAVM and DM.  
P = 500 kW.

In both models, the fundamental current magnitude increases with the reduction of pf. This happens due to the increase of the total current injected into the grid when real power (P) is kept constant. The HAVM and DM do not match on the third-order harmonic. This is the result of a larger unbalance in the switching of the HAVM. This yields differences in the results of the triplen harmonics. The fifth-order harmonic, which is the dominant current harmonic, also increases with the reduction of pf. The HAVM fifth-order harmonic magnitudes match closely with those of the DM.

The phase angles of the fundamental and fifth-order harmonic currents change with the reduction of pf. As the power factor is reduced, the phase

	$\angle I_{L,pk}$ with pf = 1 [°]		$\angle I_{L,pk}$ with pf = 0.9 [°]	
h	HAVM	DM	HAVM	DM
1	-20.72	-26.23	-41.02	-46.59
3	-34.87	79.31	-36.23	77.89
5	-82.13	-87.11	-90.04	-95.39
	$\angle I_{L,pk}$ with pf = 0.8 [°]		$\angle I_{L,pk}$ with pf = 0.7 [°]	
h	HAVM	DM	HAVM	DM
1	-49.73	-54.91	-56.24	-61.01
3	-35.00	76.37	-37.28	66.38
5	-93.58	-98.34	-98.59	-102.43

Table 4.2: Odd harmonic current phase angles of HAVM and DM.  
P = 500 kW.

angles become more negative. This means that the currents increase the lag w.r.t the Thevenin voltage source. Both models' harmonic currents interact similarly with the grid.

## Chapter 5

# Harmonic Diversity Simulation

The models introduced in Chapter 3 and 4 are put to the test in a circuit with multiple IBGs. The detailed switched model of Section 2.2 is used as a benchmark since it is the model that more accurately represents a VSC with actual switches.

Next, the harmonic simulation and comparison of the HAVM from Section 4.1 and the ACSM of Section 3.2 are performed using EMTP-RV 4.0.2.

The specifications of the hardware on which the simulations are run are as follows:

- Processor: 8-Core Processor 4.3GHz
- Memory: 16GB (2x8GB) DDR4 DRAM 3000MHz
- Hard drive: NAND 250GB Internal PC SSD - SATA III 6 Gb/s, M.2 2280.

### 5.1 69-kV Test Circuit Description

The 69-kV test circuit helps to introduce the harmonic simulation of IBGs using the HAVM, and ACSM. Figure 5.1 shows the basic circuit



schematic. The circuit model comprises two IBGs separated by an overhead transmission line (Partridge) with a length of 100 miles. The line parameters are  $R = 0.385 \frac{\Omega}{\text{miles}}$ ,  $X_L = 0.465 \frac{\Omega}{\text{miles}}$ , and  $X_C = 0.1074 \frac{\text{M}\Omega}{\text{miles}}$ .

Transformers of 1000 kVA with  $X_{fmr} = 3\%$  and  $n = \frac{69 \text{ kV}}{265 \text{ kV}}$  are connected between BUS1 and BUSINV1 to connect IBG1 to the grid and also between BUS2 and BUSINV2 to connect IBG2 to the grid; both transformers use the delta-wye grounded configuration.

The system strength at BUS1 (POI) is 2000 MVA, equivalent to an inductance of 6.31 mH at 69 kV. A three-phase load is connected at BUS1 with  $P_{3\phi} = 0.2500 \text{ MW}$  and  $Q_{3\phi} = 0.1065 \text{ Mvar}$ . Another load is connected to BUS2 with  $P_{3\phi} = 0.6000 \text{ MW}$  and  $Q_{3\phi} = 0.2900 \text{ Mvar}$ . Measurements are taken in all models to compare the output currents of each IBG. Currents injected into BUS1 (POI) are analyzed, as shown in Figure 5.2. The effects of harmonic phase angle diversity of currents injected into BUS1 are studied.

## 5.2 Harmonic Diversity Simulation Using the Harmonic Average Value Model

The 69-kV circuit of Figure 5.1 is created in EMTP-RV by modeling IBGs with HAVMs. HAVMs in this circuit use the current-mode control of Section 2.6.4, and have LC filters with parameters  $L_i = 80\mu\text{H}$  and  $C_f = 1500\mu\text{F}$ . IBG1 is connected to BUSINV1 and set to 500 kW while IBG2 is connected to BUSINV2 and set to generate 333 kW. Both IBGs operate at unity power factor. The buses BUSINV1 and BUSINV2 have a base voltage

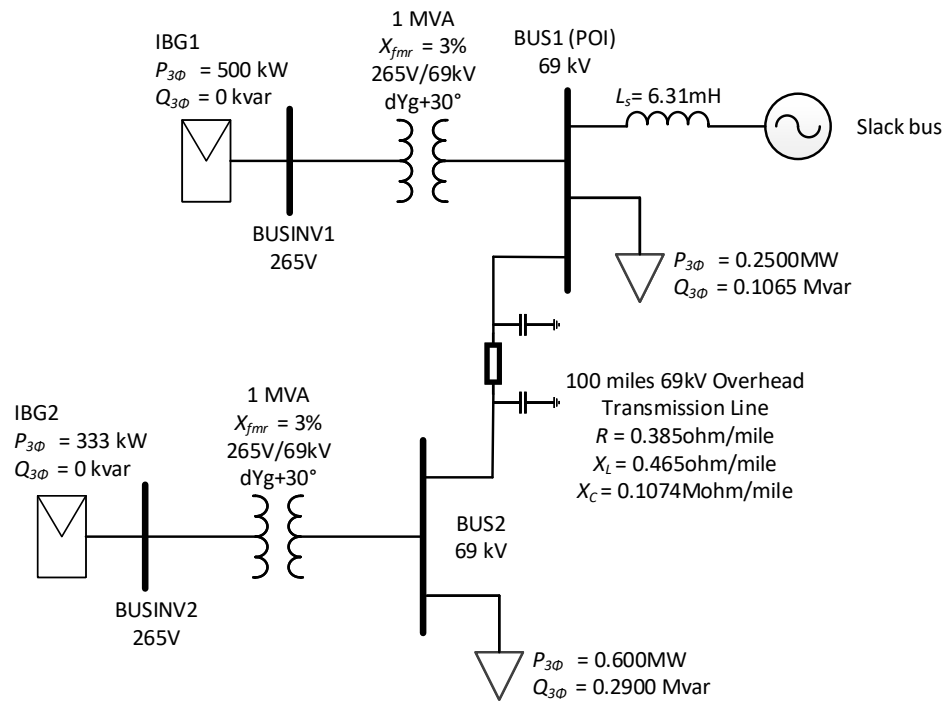


Figure 5.1: 69-kV test circuit with two IBGs and a long transmission line.

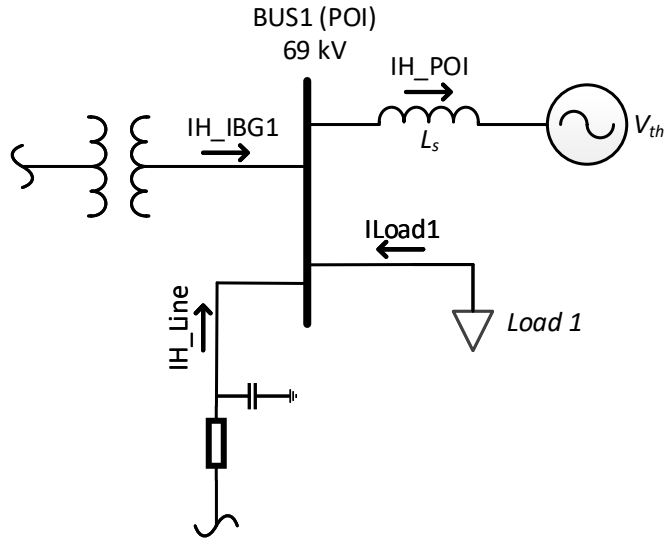


Figure 5.2: Current measurements at BUS1

of 265 V.

Figure 5.3 shows the EMTP-RV circuit model of the 69-kV test circuit. The simulation time is set to 5 s, and the time step to 5  $\mu$ s. The total simulation run-time using the HAVM is 49.82812 s.

A DM also in current-mode control was built using the same characteristics of the 69-kV test circuit to validate the HAVM. The simulation run-time for the DM is 61.38281 s, meaning the HAVM is 1.23 times faster than the DM.

Figure 5.4 shows the current measurements at the low voltage side of the transformers in both the DM and HAVM. It can be observed that the HAVM current is slightly lagging w.r.t. the DM current; this can be caused

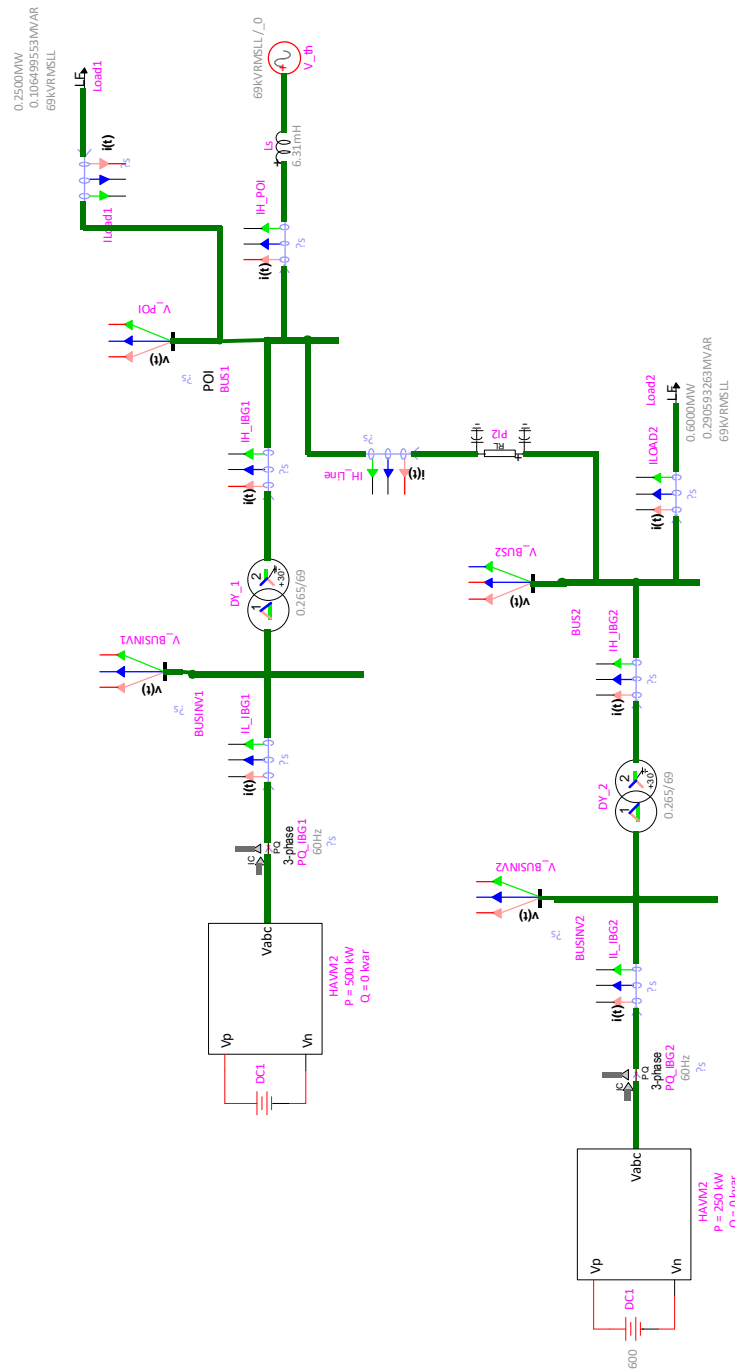


Figure 5.3: 69 kV circuit with IBGs modeled using HAVMs.

by a delay between the controller signal and the voltage source model of the HAVM. The magnitudes of the harmonic peaks seem to be similar and in phase.

Tables 5.1 and 5.2 show the harmonic current peaks and phase angles' results of IBG1 and IBG2. Current harmonics of smaller magnitude have a more substantial difference in magnitude and phase angle; they can be neglected from the analysis.

The second and third-order harmonic current magnitudes are higher in the HAVM. The presence of higher second and third-order harmonics can be interpreted as the result of a larger unbalance in the HAVM than in the DM. A well-balanced circuit will have a small second-order harmonic due to symmetry and also a small third-order harmonic due to triplens cancelation at the delta side of the transformer. The fifth-order current harmonic is dominant in both the HAVM and DM and is chosen as a reference for the harmonic analysis.

The fifth-order harmonic current probes at BUS1 (POI) are shown in Figure 5.2. Currents are assumed to flow into the POI, except  $I_{H\_POI}$ , which flows towards the Thevenin equivalent voltage source  $V_{th}$ . To demonstrate the harmonic diversity of the HAVM, (5.1) is used. This equation states that the current phasor  $I_{H\_POI(h)} \angle \theta_{H\_POI(h)}$  is the result of the sum of each current flowing to the POI at every harmonic index  $h$  including the fundamental. Thus, the resulting current phasor  $I_{H\_POI}$  could have a magnitude less than or equal to the sum of magnitudes of the current phasors injected into BUS1 (POI). If all harmonic currents are in phase at each index  $h$ , then the magnitude of

$h$	$I_{h,pk}$ [A]		Angle [°]	
	HAVM	DM	HAVM	DM
1	$1.5332 \times 10^{+03}$	$1.5152 \times 10^{+03}$	-24.7278	-27.0564
2	$2.7342 \times 10^{+00}$	$1.1566 \times 10^{+00}$	-26.7232	83.9913
3	$1.1663 \times 10^{+00}$	$7.9020 \times 10^{-01}$	-21.5135	84.6325
4	$6.8868 \times 10^{-01}$	$2.6846 \times 10^{-01}$	-60.0698	50.2900
5	$9.1698 \times 10^{+00}$	$1.2979 \times 10^{+01}$	-87.7851	-93.9853
6	$3.4594 \times 10^{-01}$	$6.8547 \times 10^{-02}$	-53.2812	69.4473
7	$4.3572 \times 10^{+00}$	$7.5659 \times 10^{-01}$	-127.1436	-153.4600
8	$4.5235 \times 10^{-01}$	$2.4056 \times 10^{-01}$	-56.9086	78.2649
9	$3.5258 \times 10^{-01}$	$1.7267 \times 10^{-01}$	-26.6779	69.0063
10	$2.0340 \times 10^{-01}$	$2.4027 \times 10^{-01}$	178.4618	83.3391

Table 5.1: Current spectra of HAVM and DM at 500 kW (IBG1).

$I_{H\_POI}$  will be equal to the sum of the harmonic peaks. On the other hand, the magnitude of  $I_{H\_POI}$  will be smaller if not all currents are in phase – this can be represented using the inequality (5.2).

$$\begin{aligned}
I_{H\_IBG1(h)} \angle \theta_{H\_IBG1(h)} + I_{H\_Line(h)} \angle \theta_{H\_Line(h)} + I_{Load1(h)} \angle \theta_{Load1(h)} \\
= I_{H\_POI(h)} \angle \theta_{H\_POI(h)} \quad (5.1)
\end{aligned}$$

$$|I_{H\_IBG1(h)}| + |I_{H\_Line(h)}| + |I_{Load1(h)}| \geq |I_{H\_POI(h)}| \quad (5.2)$$

The 69-kV test circuit has a long transmission line of 100 miles; this introduces a phase shift in the current injected by IBG2, increasing the harmonic phase angle diversity of currents injected at BUS1 (POI). This can be

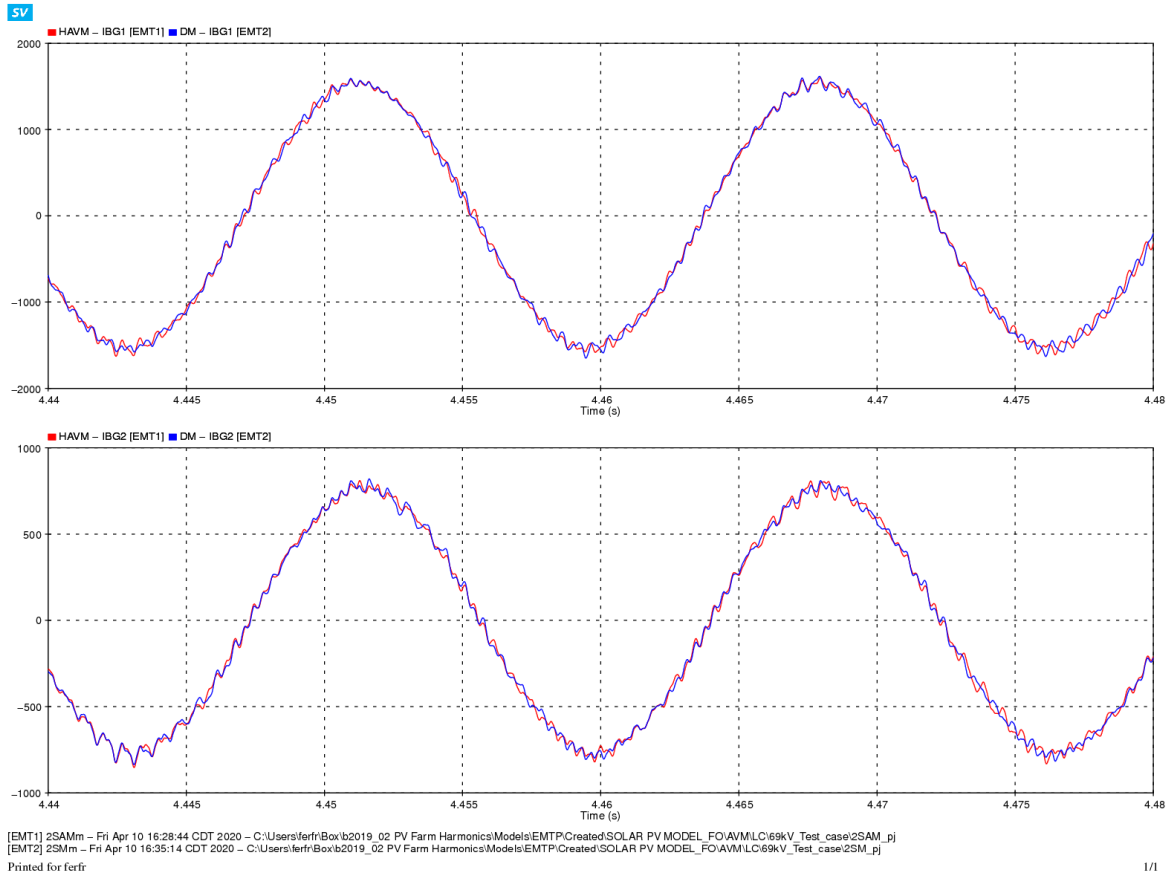


Figure 5.4: Output current waveshapes comparison: HAVM (blue) and DM (red). IBG1 (top), and IBG2 (bottom).

$h$	$I_{h,pk}$ [A]		Angle [°]	
	HAVM	DM	HAVM	DM
1	$7.6979 \times 10^{+02}$	$7.5754 \times 10^{+02}$	-27.4663	-32.1165
2	$2.1161 \times 10^{+00}$	$5.4108 \times 10^{-01}$	-39.9859	101.0850
3	$1.1530 \times 10^{+00}$	$2.6863 \times 10^{-01}$	-43.2949	83.2920
4	$9.1151 \times 10^{-01}$	$9.1428 \times 10^{-02}$	-19.5358	121.0329
5	$8.4024 \times 10^{+00}$	$1.3404 \times 10^{+01}$	-117.4345	-121.4919
6	$8.4536 \times 10^{-01}$	$1.4088 \times 10^{-01}$	-27.8942	69.4432
7	$4.4241 \times 10^{+00}$	$1.0546 \times 10^{+00}$	-165.0459	144.5829
8	$3.5040 \times 10^{-01}$	$1.4618 \times 10^{-01}$	-42.0612	172.8715
9	$2.0487 \times 10^{-01}$	$1.7641 \times 10^{-01}$	155.1923	129.2064
10	$7.2971 \times 10^{-01}$	$4.3406 \times 10^{-01}$	-7.3150	82.6378

Table 5.2: Current spectra of HAVM and DM at 250 kW (IBG2).

Branch	$I_{h=5,pk}$ [A]		Angle [°]	
	HAVM	DM	HAVM	DM
IH_Inv1	$3.1519 \times 10^{-02}$	$5.0356 \times 10^{-02}$	-119.7882	-124.6383
Iload1	$3.6650 \times 10^{-05}$	$6.1327 \times 10^{-05}$	130.3451	125.5853
IH_line	$2.8353 \times 10^{-02}$	$5.0957 \times 10^{-02}$	-155.0100	-153.5865
IH_PCC	$5.7071 \times 10^{-02}$	$9.8092 \times 10^{-02}$	-136.4743	-139.2359

Table 5.3: HAVM and DM fifth-order harmonic currents at BUS1.



observed in the angles shown in Table 5.3. The measurements show that the total current injected into the POI is smaller in the HAVM compared to the DM. This is the result of small differences in the harmonic current injected by IBG1 and IBG2 in both models. The fifth-order harmonic phase angles are very close; this shows that despite the total current magnitude, the currents are in phase in both models.

To demonstrate the harmonic diversity of the HAVM, (5.1) is used along with the currents injected into BUS1 shown in Table 5.3. The resulting current calculated with (5.1) gives the same measured value of  $I_{H\_POI}$  in EMTP-RV. This verifies that the line introduces phase angle diversity in the currents injected into BUS1 (POI) since the magnitudes of both the measured and computed values of  $I_{H\_POI}$  are smaller than the sum of magnitudes of the harmonic currents injected into BUS1.

$$\begin{aligned}
& 3.1519 \times 10^{-02} \angle -119.7882^\circ + 3.6650 \times 10^{-05} \angle 130.3451^\circ + 2.8353 \times 10^{-02} \angle -155.0100^\circ \\
& = 5.7072 \times 10^{-02} \angle -136.474^\circ \quad (5.3)
\end{aligned}$$

The HAVM achieves a faster simulation run-time and uses fewer elements compared to the DM but still requires the tuning of a filter and a controller, which can be difficult when there is not enough data from the manufacturer.

### 5.3 Harmonic Diversity Simulation Using the Automated Current Source Model

The ACSM reads harmonic currents' magnitude and phase angle data from a DWJ text file that stores data from a manufacturer's harmonic report or a detailed model's current measurements. For this simulation, the data were collected from a detailed model operating with voltage-mode control and tuned using the circuit of Figure 2.2. The DM was designed to emulate the harmonic spectra of a commercial inverter by incorporating an LCL filter adjusted to three different generation levels. Table 3.1 shows the LCL filter parameters.

ACSMs use the steady-state fundamental voltage phase angles at the inverter side of the transformers (e.g., BUSINV1 and BUSINV2) as input. This angle is computed by creating a load flow circuit; this can be modeled as a separate file or a combined time-domain load flow circuit (*TDLF*). Chapter 5 expands the simulation process by using the *TDLF* model.

To model the load flow circuit in EMTP-RV, all IBGs and loads are replaced with load flow elements. Load flow generators can be modeled as PQ-controlled (constant real and reactive power) or PV-controlled (constant real power and voltage magnitude) generators. IBGs are set to operate as PQ-controlled generators in this simulation. Figure 5.5 shows the load flow 69-kV test circuit in EMTP-RV; the resulting fundamental phase angle is  $-29.14043^\circ$  at BUSINV1 and  $-29.54584^\circ$  at BUSINV2.

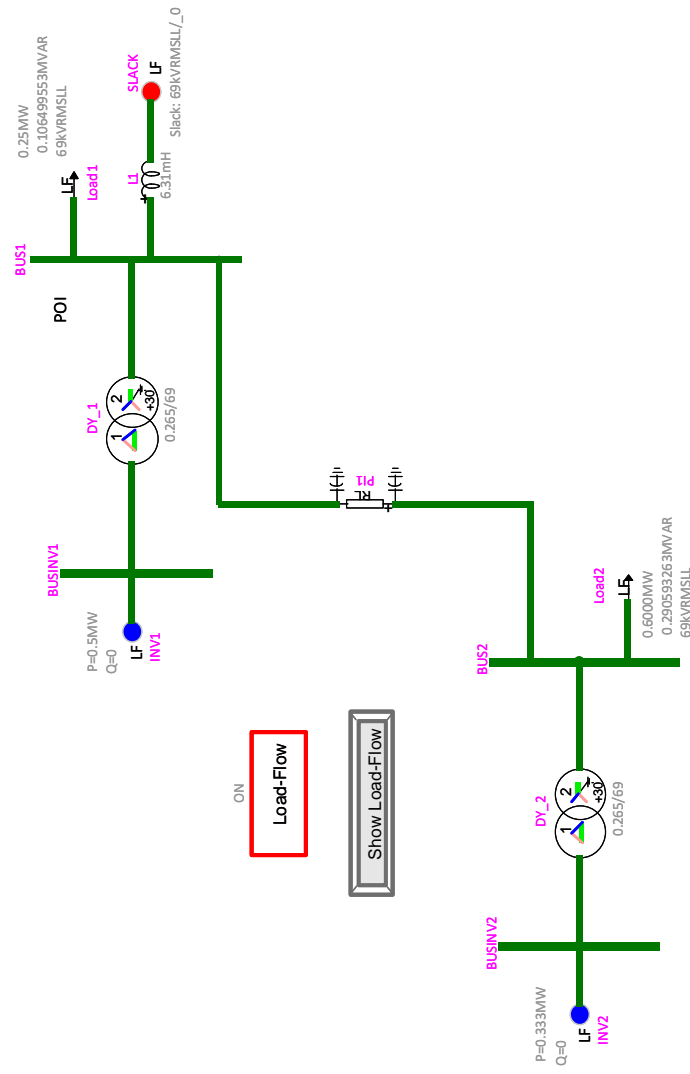


Figure 5.5: 69 kV load flow circuit.

Next, the measured phase angles are provided as inputs to the black box script of the ACSMs; this adjusts the injection of the fundamental and harmonics currents [5]. Figure 5.6 shows how to input the inverter’s phase angle, transformer configuration, and real power fraction of  $P_{rated}$  using the black box script of the ACSM in EMTP-RV.

<b>IBG1</b>	<b>IBG2</b>
<div style="font-size: small; border-bottom: 1px solid black; padding-bottom: 2px;">Use input grid for Initial Parameters-Values □</div> <div style="border-bottom: 1px solid black; padding-bottom: 2px; text-align: center; font-weight: bold;">Initial Parameters-Values: Text mode input</div> <pre style="font-family: monospace; font-size: small; margin: 0;"> Pgen_frac = 1; trans_turns_ratio = 69e3/265; trans_config = 1; // 1: DYg+30, 2: YYg inverter_bus_angle = -29.14043; </pre>	<div style="font-size: small; border-bottom: 1px solid black; padding-bottom: 2px;">Use input grid for Initial Parameters-Values □</div> <div style="border-bottom: 1px solid black; padding-bottom: 2px; text-align: center; font-weight: bold;">Initial Parameters-Values: Text mode input</div> <pre style="font-family: monospace; font-size: small; margin: 0;"> Pgen_frac = 2/3; trans_turns_ratio = 69e3/265; trans_config = 1; // 1: DYg+30, 2: YYg inverter_bus_angle = -29.54584; </pre>

Figure 5.6: ACSM black box script in EMTP-RV,  $P_{rated} = 500$  kW

The complete 69-kV test circuit with IBGs modeled as ACSMs is shown in Figure 5.7. It should be noted that the ACSMs are placed in the circuit by replacing the VSC and transformer; hence the current measurements have to be taken at the 69-kV side of the circuit. A separate file with DMs in voltage mode control is shown in Figure 5.8.

Figure 5.9 shows the current measurements at the high voltage side of the transformers in both the DM and ACSM. Both currents of the DMs and ACSMs seem to match very well and are in phase. Tables 5.4 and 5.5 show the harmonic currents of IBG1 and IBG2 respectively.

The harmonic current spectra for the ACSMs and DMs match very well at  $P_{rated} = 500$  kW. The IBG operating at two-thirds of rated power (333 kW)

$h$	$I_{h,pk}$ [A]		Angle [°]	
	ACSM	DM	ACSM	DM
1	$5.8891 \times 10^{+00}$	$5.8456 \times 10^{+00}$	0.2005	1.1930
2	$2.6218 \times 10^{-03}$	$4.6668 \times 10^{-03}$	39.1875	64.2289
3	$1.3689 \times 10^{-13}$	$3.0168 \times 10^{-03}$	-3.3971	48.4455
4	$3.2262 \times 10^{-03}$	$4.1630 \times 10^{-03}$	175.2501	100.5842
5	$2.1686 \times 10^{-01}$	$2.0303 \times 10^{-01}$	171.2599	171.9215
6	$1.4011 \times 10^{-13}$	$7.4098 \times 10^{-03}$	-11.2038	-45.9977
7	$1.0687 \times 10^{-02}$	$1.1168 \times 10^{-02}$	73.2453	75.2281
8	$1.1508 \times 10^{-03}$	$1.3695 \times 10^{-03}$	83.5668	116.6010
9	$1.5499 \times 10^{-13}$	$7.7622 \times 10^{-04}$	-27.7651	110.5865
10	$5.3746 \times 10^{-04}$	$9.0430 \times 10^{-04}$	156.1972	109.0575

Table 5.4: Current spectra of ACSM and DM at 500 kW (IBG1, rated power).

$h$	$I_{h,pk}$ [A]		Angle [°]	
	ACSM	DM	ACSM	DM
1	$3.9119 \times 10^{+00}$	$3.9262 \times 10^{+00}$	0.0475	1.3196
2	$2.3093 \times 10^{-03}$	$5.5734 \times 10^{-03}$	-51.7995	86.2918
3	$3.1246 \times 10^{-12}$	$3.1950 \times 10^{-03}$	-0.2718	104.8021
4	$2.9943 \times 10^{-03}$	$4.6655 \times 10^{-03}$	150.7576	52.7901
5	$1.9074 \times 10^{-01}$	$1.1450 \times 10^{-01}$	-50.1980	-30.1609
6	$3.1236 \times 10^{-12}$	$1.2605 \times 10^{-03}$	-0.7152	-149.9151
7	$2.7932 \times 10^{-03}$	$2.0198 \times 10^{-03}$	-26.5536	-14.2708
8	$1.9457 \times 10^{-04}$	$3.1513 \times 10^{-04}$	-85.9885	29.3363
9	$3.1240 \times 10^{-12}$	$8.8126 \times 10^{-04}$	-1.4406	71.1117
10	$1.9410 \times 10^{-04}$	$2.3214 \times 10^{-04}$	-110.2120	118.4423

Table 5.5: Current spectra of ACSM and DM at 333 kW (IBG2, two-thirds of rated power).

shows slight differences in the results; this is due to the presence of unbalanced currents in the DM.

The unbalance of the DM can be proven by analyzing the harmonic currents at multiples of the third-order harmonic (triplens) entering the delta side of the transformers; if there is a well balanced current injection at the delta side of the transformer, all triplen currents will cancel in the delta since they have zero-sequence behavior. The triplens current flowing from the delta to the wye grounded side of the transformer in the DM are not completely nullified; this is due to the slight unbalance of the switching behavior of the DM. Harmonic currents' phase angles can be neglected if the magnitudes of the harmonics are very small. The harmonic simulation of both the ACSM and the DM show a dominant fifth-order harmonic current.

The fifth-order harmonic currents injected into BUS1 (POI) were measured, as shown in Figure 5.2. Table 5.6 shows the fifth-order harmonic current measurements at the POI. Similar to the HAVM analysis, (5.1) shows that the total harmonic current flowing into the POI is equal to the phasor sum of all currents injected at BUS1.

$$\begin{aligned}
 & 2.1686 \times 10^{-01} \angle 171.26^\circ + 9.4870 \times 10^{-05} \angle 134.94^\circ + 1.8899 \times 10^{-01} \angle -51.84^\circ \\
 & = 1.5130 \times 10^{-01} \angle -130.9^\circ \quad (5.4)
 \end{aligned}$$

As expected,  $|I_{H\_POI(5)}|$  is smaller than the sum of magnitudes of harmonic current phasors injected at the POI.

Branch	$I_{h=5,pk}$ [A]		Angle [°]	
	ACSM	DM	ACSM	DM
IH_Inv1	$2.1686 \times 10^{-01}$	$2.0303 \times 10^{-01}$	171.26	171.92
Iload1	$9.4846 \times 10^{-05}$	$6.7690 \times 10^{-05}$	134.94	102.74
IH_line	$1.8899 \times 10^{-01}$	$1.1345 \times 10^{-01}$	-51.84	-31.74
IH_PCC	$1.5131 \times 10^{-01}$	$1.0907 \times 10^{-01}$	-130.19	-163.44

Table 5.6: ACSM and DM fifth-order harmonic currents at BUS1.

The simulation run-time of the ACSM was 18.28125 s while that of the DM in voltage-mode control was 46.375 s. The ACSM is 2.5 times faster than the DM. Both models used a simulation time of 5 s and a time step of 5  $\mu$ s. The ACSM simplifies most of the DM complexities – it removes the control loop, filters, and transformer. However, it requires data from the manufacturer’s harmonic report, including harmonic current magnitudes and phase angles at different generating set points and system strengths. Data from harmonic current magnitudes are readily available from manufacturers, but phase angles are seldom included in their reports. Thus, if manufacturers provide complete information about their VSC harmonic spectra, the ACSM could be an excellent alternative to simulate harmonics in power systems.

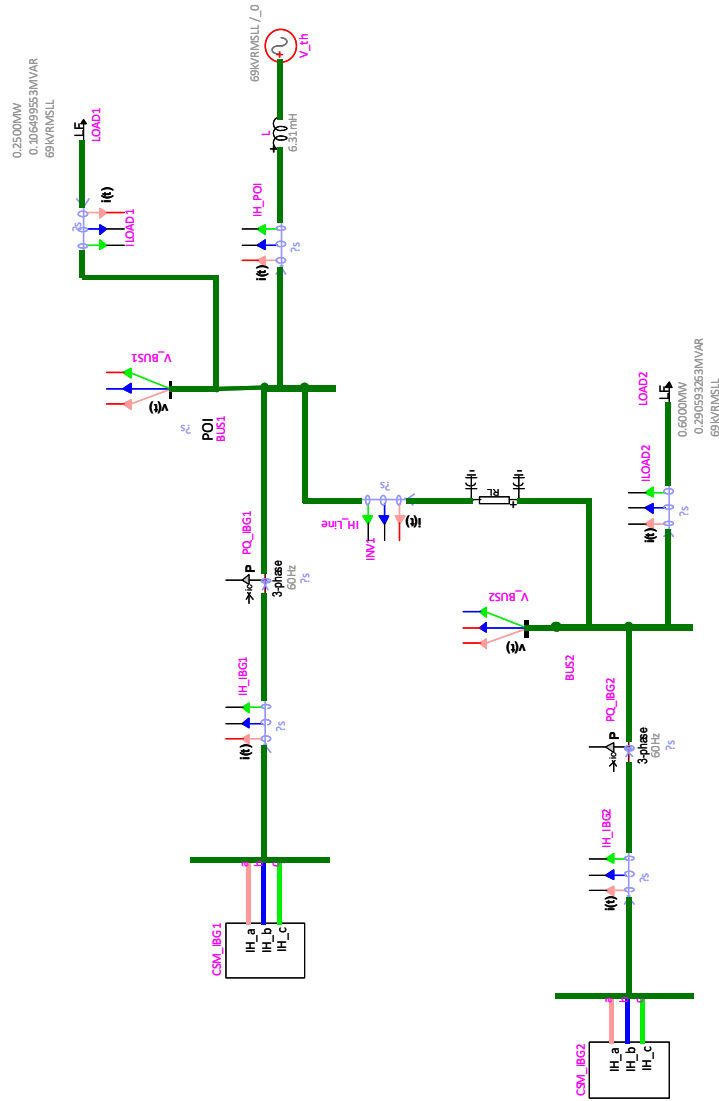


Figure 5.7: 69-kV circuit with IBGs modeled using ACSMs.



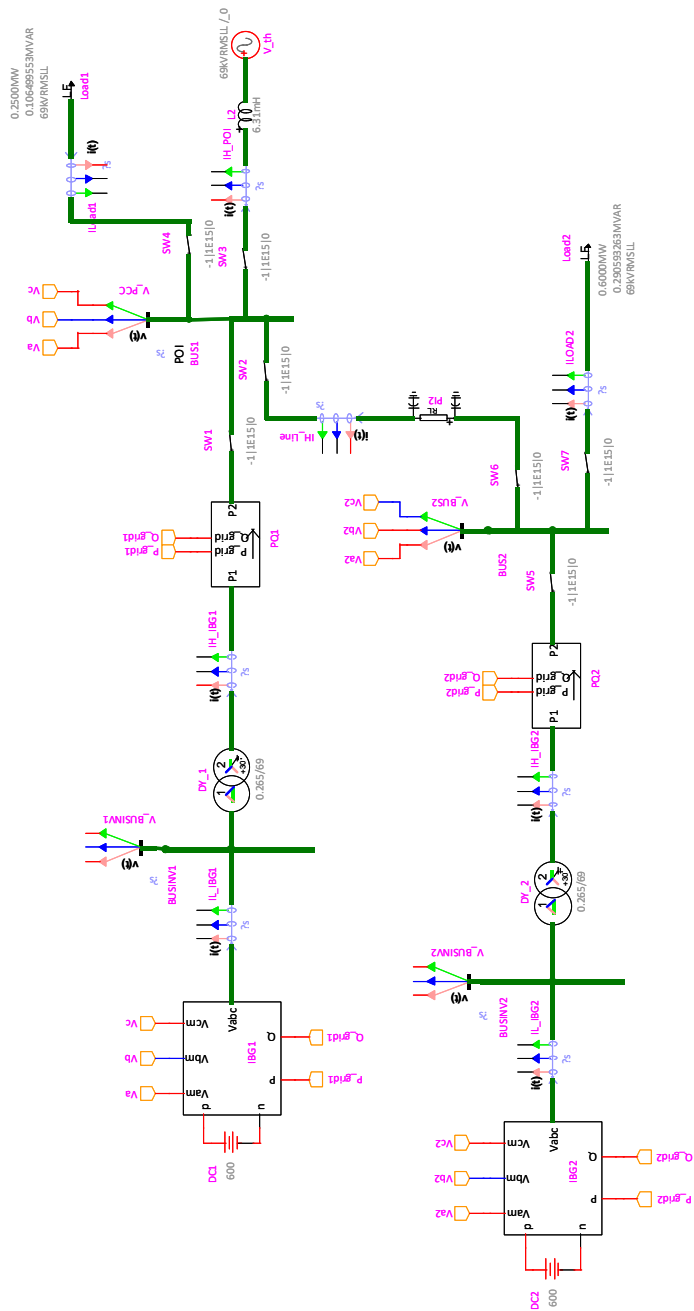


Figure 5.8: 69-kV circuit with IBGs modeled using DMs in voltage-mode control.

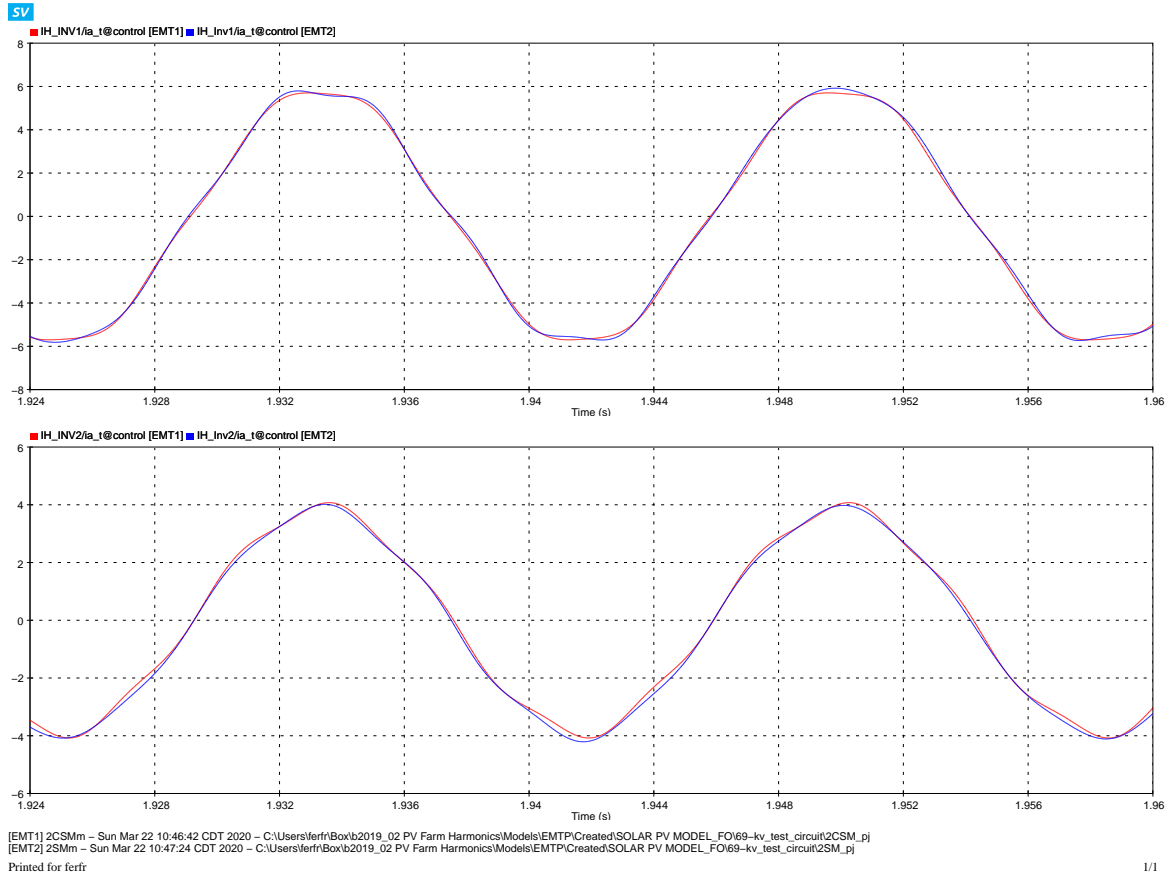


Figure 5.9: Output current waveshapes comparison: ACSM (blue) and DM (red). IBG1 (top), and IBG2 (bottom).

## Chapter 6

# Harmonics Diversity Simulation in Large-Scale Power Systems

This chapter applies the ACSM developed in [5] to model IBGs in a power system with multiple generators. This procedure was developed in [20, 21]. The power system studied in this chapter comprises multiple conventional generators, IBGs, and unbalanced loads. The circuit nominal voltage is 230 kV.

### 6.1 Modeling of Solar Farms in Transmission Systems

Since inverters in a solar farm are closely located to each other, they operate at almost the same generation level (due to similar solar irradiation). Moreover, being in electrical proximity to each other makes the corresponding harmonic current phase angles of the inverters almost equal. Thus, the harmonic current diversity due to multiple inverters in a solar farm is likely negligible.

Inverters are designed to meet the IEEE Standard 1547-2018 [12] harmonic limits at the rated generation level. Therefore, commercial solar inverters are considerably more likely to produce harmonic currents close to the

published harmonic limits. Harmonic currents produced by a solar farm of 20 MW, for example, are obtained by directly using the ACSM spectrum with the rated generation level increased from 500 kW to 20 MW; this means that 40 inverters of 500 kW each, can be assumed to be aggregated together and operating at the same generation level.

The solar farm can be modeled at rated, two-thirds, and one-third of the rated power. These three levels use the data of harmonic current percentages and phase angles from the corresponding levels of the 500 kW ACSM; these data are obtained from the DM of section 3.3.

Let us consider two cases:

- (i) A solar inverter of 500 kW operating at two-thirds of its rated power (333 kW).
- (ii) A scaled solar farm of 20 MW operating at two-thirds of its rated power (13.33 MW).

The output current waveforms of the two cases are shown in Figure 6.1. The current waveshape of the scaled 20 MW solar farm is identical to that of the 500 kW inverter but multiplied by a factor of  $\sim 40$ , which is the number of inverters assumed to be aggregated in the solar farm.

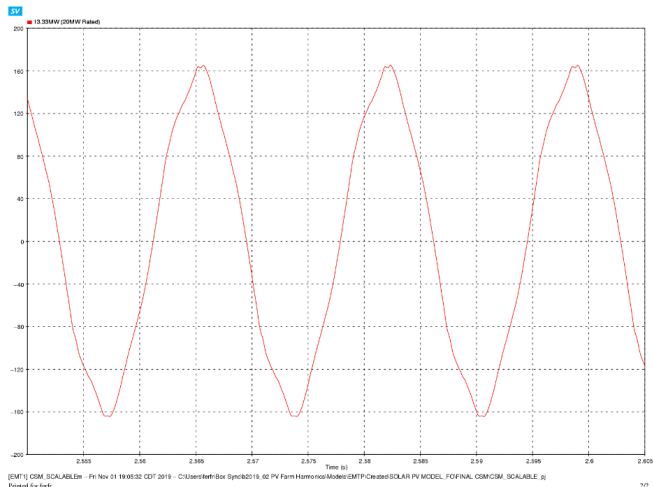
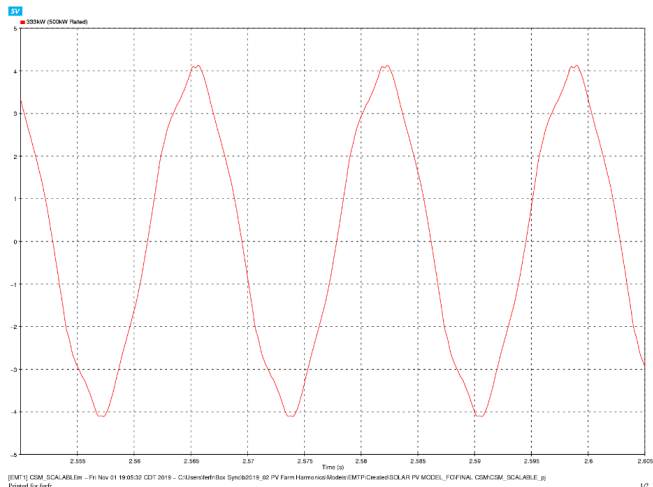


Figure 6.1: Current output of: (i) 500 kW solar inverter (top), and (ii) 20 MW solar farm (bottom).

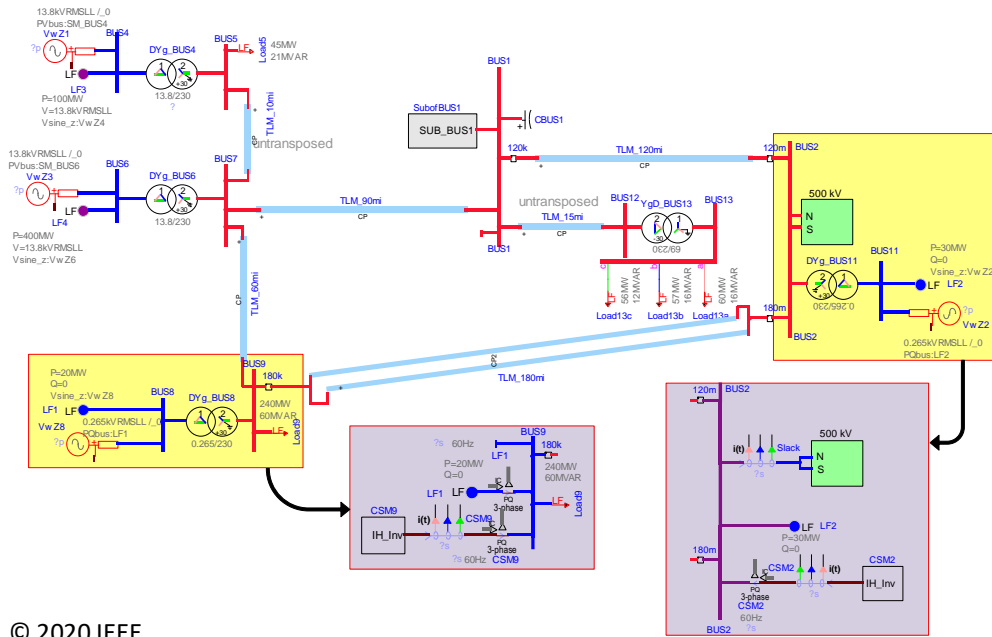
## 6.2 Circuit Simulations with Multiple ACSMs

To study the effect of harmonic current diversity due to multiple IBGs, a 13-bus example circuit in EMTP-RV is used as the base case (referred to as the *base\_ckt* for subsequent discussion). Network simulation models are built by modifying *base\_ckt* by replacing some of its conventional power plants with IBGs. Since the circuit includes multiple conventional PV-controlled buses, a steady-state load flow (LF) simulation needs to be carried out before the time-domain simulation for harmonic study. The LF simulation obtains and assigns the phase angles of the equivalent voltage sources used to represent the PV-controlled elements in the time-domain simulation.

Thus, a network simulation model is created by combining the load-flow and time-domain elements. This is called a *time-domain/load flow (TDLF)* model. Figure 6.2 shows both *base\_ckt* and its *TDLF* network simulation model. The conventional power plants in *base\_ckt* are represented by ideal voltage sources along with their equivalent synchronous reactances ( $X_d$ ); this is done to avoid the injection of third-order harmonic currents into the grid by synchronous machine models in EMTP-RV.

Three PV-controlled buses are included in *base\_ckt*: BUS 3, BUS 4, and BUS 6. The inductor data (for  $X_d$ ) of the different generator plants, along with their power and voltage settings are shown in Table 6.1. The elements highlighted in yellow in Figure 6.2, originally present in *base\_ckt*, are replaced with the elements highlighted in purple to obtain the *TDLF* model. The generator plants connected to BUS 9 and BUS 2 in *base\_ckt* are both replaced

by solar farms modeled as ACSMs in the *TDLF* model. Both ACSMs are scaled using data from the 500 kW ACSM. It should be noted that BUS 8 and BUS 11 no longer appear in the *TDLF* because they are lumped into the ACSMs at those buses, along with their respective transformers.



© 2020 IEEE

Figure 6.2: 230-kV circuit with solar farm modeled as ACSMs: elements highlighted in yellow in *base\_ckt* are replaced with elements highlighted in purple to obtain the *TDLF* model.

The *TDLF* has network elements for both steady-state (LF) and time-domain (e.g. ACSMs and conventional power plants) simulations. A combined *TDLF* model can be used for both kinds of simulations because EMTP-RV does not include LF elements in its time-domain simulations and vice-versa. Moreover, the LF elements help to determine the initial parameters of the

Generator Plant	Bus Type	$L_d$ [H]	P [MW]	$V_{LL}$ [kV]
BUS 4	PV	0.9665	100	13.8
BUS 6	PV	0.3463	400	13.8
BUS3	PV	0.9655	100	13.8
Slack	Slack	0.1133	-	500

Table 6.1: *base\_ckt* generator plant parameters and power generation.

time-domain voltage sources linked to them.

By initially performing a steady-state load flow on the *TDLF* model, the phase angles ( $\delta_{POI}$ ) at the buses with ACSMs (BUS 9 and BUS 2 in the circuit of Figure 6.2) are measured. To get the phase angles at the low voltage side of the step-up transformer ( $\delta_{inv}$ ) for buses with ACSMs,  $30^\circ$  is subtracted from measurements where the transformer has a winding configuration of delta-wye grounded, i.e.,  $\delta_{inv} = \delta_{POI} - 30^\circ$ . For wye-wye grounded transformers, no change is required, i.e.  $\delta_{inv} = \delta_{POI}$ . The power generation of ACSM depends on the value of  $\delta_{inv}$ . Next, a time-domain simulation is carried out with  $\delta_{inv}$  fed to the ACSMs. To validate the *TDLF* model, the voltages and currents of interest are measured and compared to those from *base\_ckt*. After successfully validating the *TDLF* network simulation model, harmonic diversity at BUS 2 (500 kV - Slack, subsequently referred to as Slack for simplicity) is studied.

Two network simulation models are discussed below, with IBGs rated at 30 MW and 100 MW, respectively. The 100 MW circuit contains additional reactive power compensation elements to maintain voltages within acceptable limits.



### 6.2.1 Model with Solar Farms Rated at 30 MW

In this model, the solar farm at BUS 2 is set to 30 MW (rated power) at unity power factor, and the one at BUS 9 is set to 20 MW (two-thirds of the rated power) at unity power factor. The voltages from a steady-state load flow simulation on *base\_ckt* and a time-domain (TD) simulation on the ACSM *TDLF* are shown in Table 6.2, and are found to be reasonably close to each other. Thereby, the ACSM representation of the solar farms in this circuit is validated. Since BUS 8 and BUS 11 no longer exist in the *TDLF*, their voltages are marked as N/A for the ACSM TD in Tables 6.2.

Next, harmonic diversity at BUS 2 (Slack) is evaluated. The branches connected to BUS 2 are shown in Figure 6.3 and the injected harmonic currents at BUS 2 are shown in Table 6.3 and Table 6.4. As can be seen, the fifth-order harmonic is the most significant one in the network. The total fifth harmonic current flowing into Slack is the sum of the individual fifth harmonic current injections from each branch. The peak of the fifth-order harmonic current flowing into Slack is found to be greater than that injected by ACSM2, but smaller than the arithmetic sum of the peaks of the injected fifth-order harmonic currents.

	$V_{base,LL}$	$base\_ckt$		ACSM TD	
Bus	[kV]	V [pu]	Angle [deg]	V [pu]	Angle [deg]
1	230.000	1.030	23.640	1.025	23.400
2	230.000	1.010	16.010	1.012	15.950
3	13.800	1.000	-2.240	1.003	-2.390
4	13.800	1.000	9.220	1.003	8.970
5	230.000	0.990	34.400	0.992	34.090
6	13.800	1.000	8.840	1.003	8.580
7	230.000	0.990	34.030	0.993	33.710
8	0.265	0.970	-0.840	N/A	N/A
9	230.000	0.970	24.120	0.970	23.810
10	500.000	1.000	12.960	1.000	12.960
11	0.265	1.010	-9.090	N/A	N/A
12	230.000	1.010	22.130	1.011	21.900
13	69.000	0.970	46.880	0.971	46.750

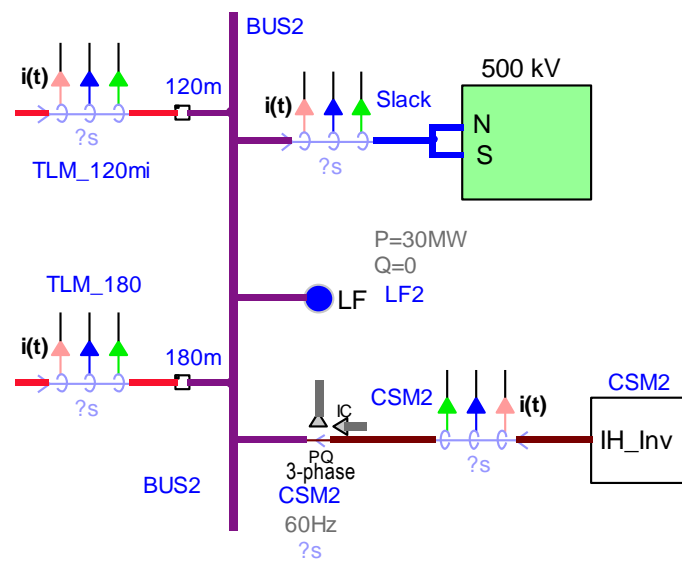
Table 6.2: Results from  $base\_ckt$  Load Flow and 30 MW-Rated ACSM Time Domain (TD,  $h = 1$ ) Simulations - No Reactive Power Compensation.

$h$	$ I_{ACSM2,pk} $ [A]	$ I_{Slack,pk} $ [A]	$ I_{TLM.120,pk} $ [A]	$ I_{TLM.180,pk} $ [A]
2	$2.2 \times 10^{-01}$	$9.6 \times 10^{-02}$	$1.4 \times 10^{-01}$	$8.1 \times 10^{-02}$
3	$1.1 \times 10^{-07}$	$8.4 \times 10^{-05}$	$4.5 \times 10^{-05}$	$3.9 \times 10^{-05}$
4	$1.3 \times 10^{-01}$	$8.9 \times 10^{-02}$	$9.4 \times 10^{-02}$	$8.2 \times 10^{-02}$
5	$3.6 \times 10^{00}$	$4.9 \times 10^{00}$	$1.3 \times 10^{00}$	$2.8 \times 10^{00}$

Table 6.3: Harmonic current magnitudes at BUS 2. Circuit with 30 MW rated solar farms (without reactive power compensation).

$h$	$\angle I_{ACSM2,pk}$ [°]	$\angle I_{Slack,pk}$ [°]	$\angle I_{TLM.120,pk}$ [°]	$\angle I_{TLM.180,pk}$ [°]
2	69.5317	-3.1905	-93.5074	-70.8111
3	178.3718	-36.0315	-32.2674	-40.2325
4	-124.0617	-144.9614	31.1643	175.7825
5	-112.8797	-105.2125	99.9022	-83.3092

Table 6.4: Harmonic current phase angles at BUS 2. Circuit with 30 MW rated solar farms (without reactive power compensation).



© 2020 IEEE

Figure 6.3: Current measurement sources at BUS 2. Circuit with 30 MW rated solar farms (without reactive power compensation).

### 6.2.2 Model with Solar Farms Rated at 100 MW

For this model, the base circuit is modified to have a generation level of 100 MW at BUS 9 and 66.67 MW at BUS 2. Accordingly, the rated power of both solar farms is increased to 100 MW. The current spectra of the solar farms at BUS 9 and BUS 2 are interchanged from the previous case to increase the harmonic diversity of the circuit – ACSM9 and ACSM2 are set to operate at 100 MW (rated power) and 66.67 MW (two-thirds of the rated power) respectively. Due to high power generation levels, reactive power compensations of 23.09 Mvar and 39.28 Mvar are required at BUS 2 and BUS 9, respectively, to maintain their voltages close to 1 pu in the *TDLF* model. The required reactive power is supplied by adding a capacitor of 1.1576  $\mu\text{F}$  at BUS 2 and a capacitor of 1.9694  $\mu\text{F}$  at BUS 9. These capacitors are also added to the modified base circuit, now referred to as *base\_ckt\_modified*. No other change is made to the circuit topology.

The results from a steady-state load flow simulation on *base\_ckt\_modified* and a time-domain simulation on the ACSM *TDLF* are shown in Table 6.5, and are found to be reasonably close. Thereby, the ACSM representation of the solar farms in this circuit is validated. The *base\_ckt\_modified* includes transformers that consume reactive power, whereas transformers are inherently assumed to be ideal when lumped into the ACSMs of the *TDLF*. This difference causes a noticeable deviation between the voltages in Table 6.5 for buses close to the solar farms, especially BUS 9.

Finally, harmonic diversity at BUS 2 (Slack) is evaluated. The branches

Bus	$V_{base,LL}$	<i>base_ckt_modified</i>		ACSM TD	
	[kV]	V [pu]	Angle [deg]	V [pu]	Angle [deg]
1	230.000	1.018	28.630	1.024	28.360
2	230.000	1.005	17.930	1.013	17.950
3	13.800	1.000	2.790	1.002	2.450
4	13.800	1.000	16.660	1.002	15.940
5	230.000	0.990	41.820	1.000	41.200
6	13.800	1.000	16.280	1.002	15.560
7	230.000	0.991	41.450	1.001	40.830
8	0.265	0.854	32.540	N/A	N/A
9	230.000	0.959	33.090	1.005	32.680
10	500.000	1.000	12.960	1.000	12.960
11	0.265	0.993	-0.960	N/A	N/A
12	230.000	1.004	27.110	1.011	26.850
13	69.000	0.966	51.760	0.974	51.630

Table 6.5: Results from *base\_ckt\_modified* Load Flow and 100 MW-Rated ACSM Time Domain (TD,  $h = 1$ ) Simulations - with Reactive Power Compensation.

$h$	$ I_{ACSM2,pk} $ [A]	$ I_{Slack,pk} $ [A]	$ I_{TLM.120,pk} $ [A]	$ I_{TLM.180,pk} $ [A]	$ I_{C2,pk} $ [A]
2	$5.7 \times 10^{-01}$	$9.7 \times 10^{-01}$	$2.4 \times 10^{-01}$	$2.6 \times 10^{-1}$	$2.7 \times 10^{-2}$
3	$1.4 \times 10^{-07}$	$2.7 \times 10^{-05}$	$2.5 \times 10^{-05}$	$1.0 \times 10^{-5}$	$4.6 \times 10^{-6}$
4	$5.2 \times 10^{-01}$	$4.9 \times 10^{-01}$	$3.6 \times 10^{-01}$	$2.5 \times 10^{-1}$	$5.5 \times 10^{-2}$
5	$1.1 \times 10^{+01}$	$7.7 \times 10^{00}$	$9.9 \times 10^{-01}$	$6.4 \times 10^{00}$	$1.3 \times 10^{00}$

Table 6.6: Harmonic current magnitudes at BUS 2. Circuit with 100 MW rated solar farms (with reactive power compensation).

$h$	$\angle I_{ACSM2,pk}$ [°]	$\angle I_{Slack,pk}$ [°]	$\angle I_{TLM\_120,pk}$ [°]	$\angle I_{TLM\_180,pk}$ [°]	$\angle I_{C2,pk}$ [°]
2	-16.770	7.152	18.695	51.614	6.859
3	-1.620	9.577	24.937	-41.250	174.416
4	-139.183	-160.350	55.824	-154.206	-160.527
5	37.376	57.168	-23.876	-170.894	57.045

Table 6.7: Harmonic current phase angles at BUS 2. Circuit with 100 MW rated solar farms (with reactive power compensation).

connected to BUS 2 are shown in Figure 6.4 and the injected harmonic currents at BUS 2 are shown in Table 6.6 and Table 6.7. This circuit has an additional branch current flowing into the capacitor C2, as shown in Figure 6.4. Like the previous case, the fifth-order harmonic is the most significant. The total harmonic current flowing into Slack is the sum of the individual harmonic currents of each branch. Unlike the previous case, the peak fifth harmonic current flowing into Slack is found to be even smaller than that injected by ACSM2. This happens due to partial cancellation of the fifth harmonic current from ACSM2 by the fifth harmonic currents injected from other branches.

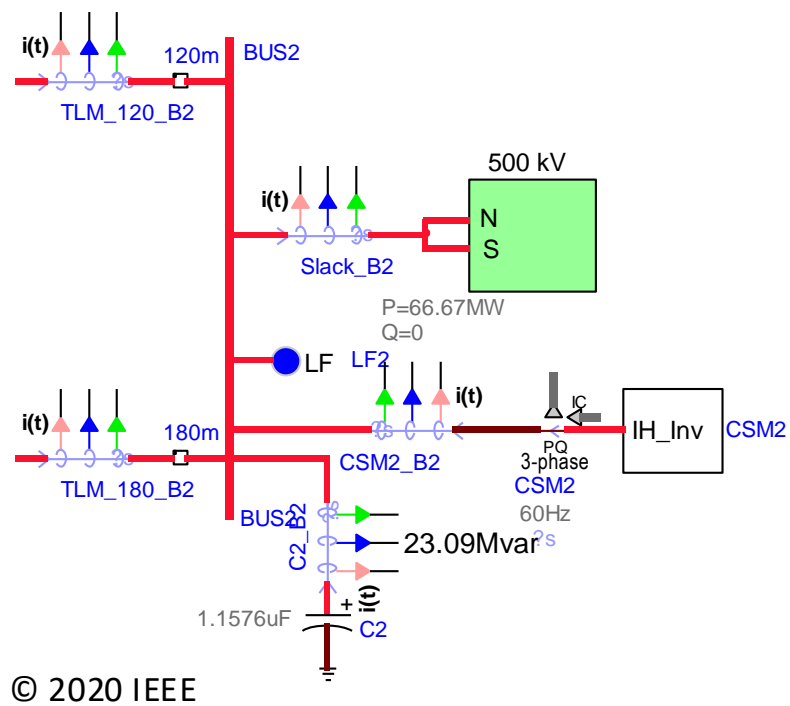


Figure 6.4: Branches at BUS 2. Circuit with 100 MW rated solar farms (with reactive power compensation).

## Chapter 7

### Conclusion and Future Work

#### 7.1 Conclusion

The study of multiple IBG models in this thesis led to the development of new techniques to study the harmonic currents' interaction with the grid. These currents are the result of the modulation schemes used on power electronic devices, which cause adverse effects on the power system. The harmonic currents are sensitive to the grid characteristics and controller parameters. Furthermore, the generation set-point and power factor of the IBGs affect the harmonic current magnitudes and phase angles.

The studied automatic current source model offers a simplified yet flexible way to study harmonic currents in power systems. The ACSM can read harmonic data contained in DWJ files; these data have information of harmonic current magnitudes and phase angles.

The ACSM outperformed the DM by considerably reducing the simulation time in circuits with multiple IBGs. If data regarding harmonic current magnitudes and phase angles at different system strengths happen to be available from manufacturers, the ACSM might be a great alternative to model IBGs during the planning phase. However, the ACSM did not capture the



unbalanced current injection of the DM since it assumes the currents to be balanced in all phases; besides, the IBG's transformer is modeled as ideal. This leads to a total cancellation of the triplen harmonics in the circuit. Moreover, some harmonics of small magnitudes were having differences in their results.

The HAVM works in a similar manner as the DM and incorporates the same filter and controller. This increases the circuit complexity and run-time, considering that circuits with more components show in general longer run-times. Thus, the HAVM does improve the run-time in simulations with multiple IBGs, but the ACSM is still faster and simpler. Further, the HAVM requires the user to tune the controller and filter, which is almost equivalent to tuning the DM. The HAVM modeled in this thesis achieved good results on the fundamental and fifth-order harmonic currents. However, the results in the HAVM are less conservative than the ACSM since the total harmonic current injected at the POI resulted in a smaller magnitude compared to the DM and ACSM.

Due to the complexity of the HAVM, the ACSM was chosen to perform harmonic diversity simulation in power systems with multiple conventional generators. Different results were obtained from test cases studied in Chapter 5. The test case with reactive power compensation was found to have a larger harmonic current cancellation at the POI, meaning that changes in the circuit and the generators set-points can affect the total harmonic current injected at the POI. This is due to the harmonic current phase angle diversity that is successfully captured by the ACSM.

It is observed that the total harmonic current injected into the POI changes its magnitude depending on the harmonic angle diversity of the circuit. There are two possible outcomes on harmonic simulations: (i) The POI harmonic current magnitude is almost equal to the sum of magnitudes of the harmonic currents injected into the POI. (ii) The POI harmonic current magnitude is noticeably less than the sum of magnitudes of harmonic currents injected into the POI. The first outcome happens in circuits with low harmonic phase angle diversity, while the second happens in circuits with harmonic currents that are phase-shifted due to the topology of the network.

## 7.2 Future Work

Based on the models' limitations and performances, future work described in this section aims to improve the models' run-times, accuracy, and flexibility.

- The studied ACSM can be improved by including intermediate generating set-points. Data can also be collected with the IBG generating power with a pf below unity. Ideally, data should be available for any arbitrary generating set-point of an IBG.
- The ACSM can incorporate a closed-loop controller; this will be beneficial in transient simulations. The harmonic current response to transients would bring insights on how to do harmonic distortion mitigation during faults.

- The ACSM data can include information about phases a, b, and c. In this way, the ACSM would be able to simulate the DM unbalanced currents.
- Detailed ACSM models would include parallel impedances connected to their current source terminals. Modeling impedances that can only interact with one determined frequency is complicated in EMTP-RV. Finding an alternative simulator with this characteristic might help in modeling a better ACSM.
- The study of a different HAVM [4] might give better run-time results without sacrificing the accuracy of the model.
- The use of the nearest level control (NLC) could give better results when modeling IBGs using the HAVM.
- The automatic tuning of controllers and filters parameters on the HAVM and DM is a great way to make both models more user friendly. This will help to the use of the models in more complicated power systems, without the hassle of tuning all elements.

## Appendices

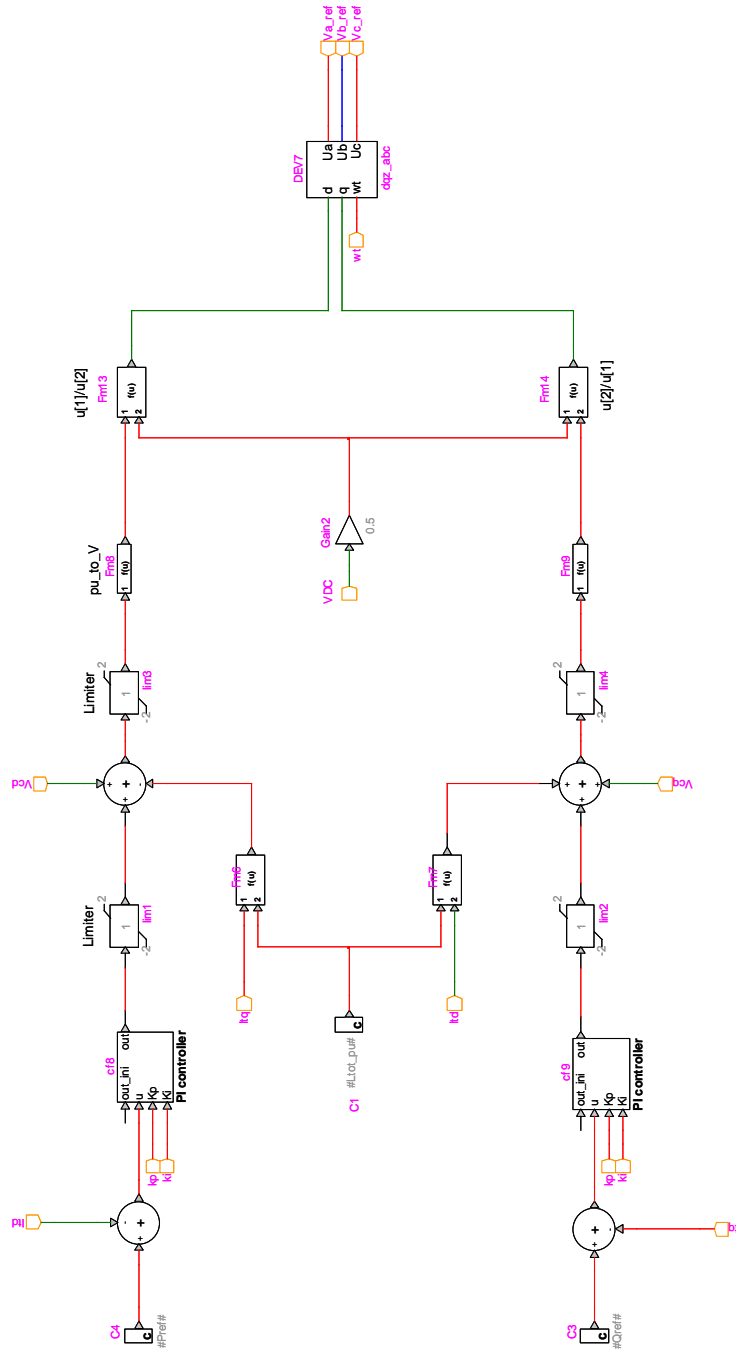


Figure 1: Current-mode control in EMTP-RV

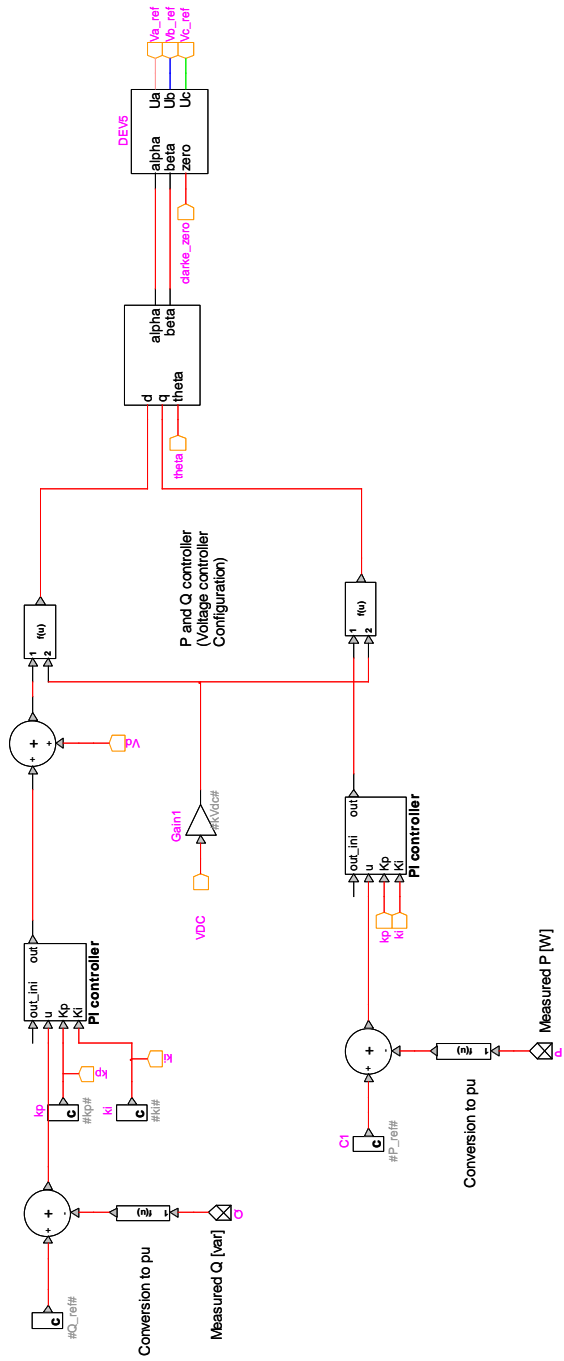


Figure 2: Voltage-mode control in EMTP-RV

## Bibliography

- [1] N. Mohan, T. M. Undeland, and W. P. Robbins, *Power Electronics: Converters, Applications, and Design*,. NJ: Wiley, 2003.
- [2] A. Yazdani, A. R. Di Fazio, H. Ghoddami, M. Russo, M. Kazerani, J. Jatskevich, K. Strunz, S. Leva, and J. A. Martinez, “Modeling guidelines and a benchmark for power system simulation studies of three-phase single-stage photovoltaic systems,” *IEEE Transactions on Power Delivery*, vol. 26, no. 2, pp. 1247–1264, April 2011.
- [3] J. Peralta, H. Saad, S. Denetiere, J. Mahseredjian, and S. Nguefeu, “Detailed and averaged models for a 401-level mmc-hvdc system,” in *2013 IEEE Power Energy Society General Meeting*, July 2013, pp. 1–1.
- [4] G. Todeschini, S. Balasubramaniam, and P. Iqic, “Time-domain modeling of a distribution system to predict harmonic interaction between pv converters,” *IEEE Transactions on Sustainable Energy*, vol. 10, no. 3, pp. 1450–1458, July 2019.
- [5] S. Roy, F. Osorio, S. Santoso, and R. Arritt, “Modeling of Inverter-Based Resources Using Equivalent Current Sources in EMTP-RV,” in *2020 IEEE Power Energy Society General Meeting*, 2020, pp. 1–1, accepted.

- [6] A. Yazdani and R. Iravani, *Voltage-Sourced Converters in Power Systems*. Wiley-Blackwell, 2010.
- [7] J. Rodriguez, Jih-Sheng Lai, and Fang Zheng Peng, “Multilevel inverters: a survey of topologies, controls, and applications,” *IEEE Transactions on Industrial Electronics*, vol. 49, no. 4, pp. 724–738, Aug 2002.
- [8] T. Ngo and S. Santoso, “Grid-connected photovoltaic converters: Topology and grid interconnection,” *AIP Journal of Renewable and Sustainable Energy*, vol. 6, no. 3, 2014.
- [9] M. Reza, J. G. Slootweg, P. H. Schavemaker, W. L. Kling, and L. van der Sluis, “Investigating impacts of distributed generation on transmission system stability,” in *2003 IEEE Bologna Power Tech Conference Proceedings*, vol. 2, June 2003, pp. 7 pp. Vol.2–.
- [10] V. Telukunta, J. Pradhan, A. Agrawal, M. Singh, and S. G. Srivani, “Protection challenges under bulk penetration of renewable energy resources in power systems: A review,” *CSEE Journal of Power and Energy Systems*, vol. 3, no. 4, pp. 365–379, Dec 2017.
- [11] D. Maheswaran, A. Kalyanasundaram, and S. Kameshwaran, “Power quality issues in a distribution network impact of neutral current due to nonlinear loads,” in *2006 India International Conference on Power Electronics*, Dec 2006, pp. 150–155.



- [12] *IEEE Standard for Interconnection and Interoperability of Distributed Energy Resources with Associated Electric Power Systems Interfaces*, Std., April 2018.
- [13] B. Liu and B. Song, “Modeling and analysis of an lcl filter for grid-connected inverters in wind power generation systems,” in *2011 IEEE Power and Energy Society General Meeting*, July 2011, pp. 1–6.
- [14] S. R. Sanders, J. M. Noworolski, X. Z. Liu, and G. C. Verghese, “Generalized averaging method for power conversion circuits,” in *21st Annual IEEE Conference on Power Electronics Specialists*, 1990, pp. 333–340.
- [15] MathWorks. Tune a control system using control system tuner. [Online]. Available: <https://www.mathworks.com/help/control/ug/tuning-control-systems-with-control-system-tuner.html>
- [16] H. Yang, D. Xia, X. Zhang, and D. Xu, “Impedance modeling and stability analysis of three-phase grid-connected inverter with lcl filter in dq-frame,” in *2019 21st European Conference on Power Electronics and Applications (EPE '19 ECCE Europe)*, Sep. 2019, pp. P.1–P.10.
- [17] E. Thunberg and L. Soder, “A norton approach to distribution network modeling for harmonic studies,” *IEEE Transactions on Power Delivery*, vol. 14, no. 1, pp. 272–277, 1999.
- [18] M. Rylander and W. M. Grady, “Problems in the use of norton equivalent models for single-phase nonlinear loads,” in *IEEE PES General Meeting*,

July 2010, pp. 1–7.

- [19] J. Peralta-Rodriguez, “Dynamic Averaged Models of VSC-Based HVDC Systems for Electromagnetic Transient Programs,” Ph.D. dissertation, Univ. de Montreal, 2013. [Online]. Available: [https://publications.polymtl.ca/1237/1/2013\\_JaimePeraltaRodriguez.pdf](https://publications.polymtl.ca/1237/1/2013_JaimePeraltaRodriguez.pdf)
  
- [20] F. Osorio, S. Roy, S. Santoso, and R. Arritt, “Evaluating Harmonic Diversity of Solar Farms Using Equivalent Current Sources in EMTP-RV,” in *2020 IEEE Power Energy Society General Meeting*, 2020, pp. 1–1, accepted.
  
- [21] *Planning for Harmonic Analysis of Utility-Scale Resources on Weak Transmission Systems: Models of Inverter-based Resources for Harmonic Studies in EMTP-RV: An equivalent current source model approach*, Std.